# MAPPING OPTIMAL RECHARGE AND EXTRACTION LOCATIONS FOR GROUNDWATER RESOURCES IN SOUTHERN SINAI, EGYPT: MODELLING AND GEOPHYSICAL CONSTRAINTS

A Thesis

by

MUHAMED ELSHALKANY

BS, Suez Canal University, 2018

Submitted in Partial Fulfillment of the Requirements for the Degree of

MASTER OF SCIENCE

in

ENVIRONMENTAL SCIENCE

Texas A&M University-Corpus Christi
Corpus Christi, Texas

August 2023

MAPPING OPTIMAL RECHARGE AND EXTRACTION LOCATIONS FOR GROUNDWATER RESOURCES IN SOUTHERN SINAI, EGYPT: MODELLING AND GEOPHYSICAL CONSTRAINTS

A Thesis

by

MUHAMED ELSHALKANY

This thesis meets the standards for scope and quality of
Texas A&M University-Corpus Christi and is hereby approved.

Mohamed Ahmed, PhD
Chair

Dorina Murgulet, PhD
Committee Member

William A. Sauck, PhD
Committee Member

August 2023

# ABSTRACT

Groundwater resources are the only long-term solution for the local Bedouin community who live in southern Sinai. However, the Bedouin community as a whole lacks a basic understanding of how these resources are developed, recharged, distributed, and how to use them sustainably. The present study addresses this issue by utilizing publicly available remote sensing data and techniques to model potential groundwater recharge and extraction locations. Furthermore, the study investigates the influence of structural elements, including faults and shear zones, on the spatial distribution of these locations. To calibrate and validate remote sensing-derived results, near-surface geophysical surveys such as Vertical Electrical Sounding (VES), Seismic Refraction (SR), and Ground Penetrating Radar (GPR) were employed. The findings of this study are as follows: (1) The study area comprises 15% high potential recharge regions, 37% moderate potential recharge regions, and 47% low potential recharge regions; (2) A total of 334 locations were identified at the intersections of two or more fault/shear zone systems, representing optimal sites for drilling sustainable groundwater wells; (3) Two trends of structural elements, namely NW-SE and NE-SW, were identified in southern Sinai. The spatial distribution of these structural elements, along with surface gradient, predominantly controls groundwater accumulation by providing preferred pathways for groundwater flow; and (4) Geophysical surveys indicated that areas where two or more faults and shear zones intersected exhibited thicker and shallower saturated zones (thickness 18-23.5 m; depth 5.5-12.5 m) compared to other areas (thickness 5.5-16 m; depth 7-13 m). The comprehensive findings of this study provide valuable insights into the potential recharge and extraction locations for sustainable groundwater use in southern Sinai. Moreover, the study highlights the significance of structural elements and their spatial distribution

in controlling groundwater availability. The methodologies employed in this research can be utilized as a framework for similar studies in other regions with highly fractured basement terrains.

# DEDICATION

“Then (even after observing this) your hearts hardened and became like stones, or even harder. For surely there are some stones from which streams burst forth and some that split asunder and water issues out, and some that crash down for fear of Allah. Allah is not heedless of the things you do.” (Holy Qur’an, 2:74)

This thesis is dedicated to my beloved parents, who have been a source of inspiration and strength when I thought of giving up, and who continue to provide moral, spiritual, emotional, and financial support. Accomplishing this would make you proud of me as much as I am proud of having you as my parents. I love you, Mom and Dad.

To my brother and sister, thank you for everything you have done for me. I know you are always proud of me for doing this accomplishment. You are truly the best brother and sister I could ever have. To my devoted fiancée, my support, whose love and patience made it possible to carry this through to the end. I love you! I also dedicate this to all my diligent professors and instructors, for you have shared your knowledge and effective teaching to me. Thank you very much! To my Egyptian and American friends, and classmates who gave me advice and encouragement to finish this study, I really appreciate your words.

# ACKNOWLEDGEMENTS

First, I sincerely thank my advisor and mentor, Dr. Mohamed Ahmed, who made this work possible. His guidance, support, motivation, patience, and immense knowledge helped me throughout the research and writing of this thesis. Second, thanks to my committee members Dr. Dorina Murgulet at TAMU-CC and Dr. William A. Sauck at Western Michigan University, for their expertise, insightful comments, and support. I truly had a wonderful committee that pushed me to accomplish and surpass my goals, and I will forever appreciate this. Third, I would like to thank Dr. Abdou Abouelmagd at SCU, Dr. Sherif Mansour at PSU, Dr. Islam El-Nekhiely at SCU, Dr. Mohamed Abdelfattah at PSU, Ahmed Beshr at Chinese Academy of Sciences, Mohmed Gamal at Chinese Academy of Sciences, Islam Alaiad at SCU, and Mohamed Samir at National Authority for Remote Sensing and Space Sciences, for their help in field data collection. And lastly, I would like to thank Prof. Mohamed El-Shafei at SCU, and Prof. Ahmed Hegazi at SCU, for their support, encouragement, and advice.

This research was supported by the Society of Exploration Geophysicists (SEG) Geoscientists Without Border (GWB) (GWB2020010013) grant awarded to the Texas A&M University–Corpus Christi.

TABLE OF CONTENTS

Page

ABSTRACT ... iv

DEDICATION ... vi

ACKNOWLEDGEMENTS ... vii

TABLE OF CONTENTS ... viii

LIST OF FIGURES ... x

LIST OF TABLES ... xiii

1. INTRODUCTION ... 1

    1.1 Overview ... 1

    1.2 Freshwater in Sinai ... 5

    1.3 Challenges ... 6

    1.4 Objective ... 7

    1.5 Significance ... 8

2. STUDY AREA ... 9

    2.1 Overview ... 9

    2.2 Geologic and Structural Settings ... 9

    2.3 Hydrogeologic Setting ... 11

3. DATA AND METHODS ... 14

    3.1 Overview ... 14

    3.2 Remote Sensing Data and GIS Techniques ... 14

3.2.1 Weighted Overlay Model (WOM) ... 14

3.2.2 Model Input Data ... 15

3.2.3 Optimal Locations for Drilling Sustainable Groundwater Wells ... 22

3.3 Near-surface Geophysical Techniques (Fieldwork) ... 23

3.4 Groundwater Borehole Data ... 36

4. RESULTS ... 38

4.1 Optimal Recharge and Extraction Locations ... 38

4.2 Structural Controls on Groundwater Accumulation and Flow in Basement Terrains 42

4.2.1 Weighted Overlay Model (WOM) ... 42

4.2.2 Model Input Data ... 50

4.2.3 Optimal Locations for Drilling Sustainable Groundwater Wells ... 57

5. DISCUSSION AND CONCLUSION ... 60

5.1 Discussion ... 60

5.2 Conclusion ... 66

REFERENCES ... 69

LIST OF FIGURES

Page

Figure 1. Location map showing Egypt's location and main physiographic features. .................. 2

Figure 2. (A) Annual rainfall (mm/yr) over Egypt (Ahmed et al., 2022). .................................... 3

Figure 3. Location map of the study area (red polygon) in the Sinai Peninsula, Egypt. ................ 5

Figure 4. Topographic map of southern Sinai. ................................................................................ 9

Figure 5. Simplified geologic map of the study area (modified from Conoco, 1987)................. 10

Figure 6. Structural map showing the main structural elements in Sinai (Gaber et al., 2022; Neev, 1975). ............................................................................................................................ 11

Figure 7. Stream network over the study area. ............................................................................ 12

Figure 8. Schematic showing aquifer types and geometries within Southern Sinai's main wadies. ........................................................................................................................................ 13

Figure 9. Average annual rainfall data over the basement terrain of Southern Sinai. .................. 16

Figure 10. (A) Landsat TM band ratio color composite image (5/7: red; 5/1: green; 5/4 x 3/4: blue) over the study area. ............................................................................................................ 17

Figure 11. (A) Spatial distributions of faults and shear zones over the basement terrain of Southern Sinai. ............................................................................................................................ 19

Figure 12. Fault density map in Km/Km$^2$ over the basement terrain of Southern Sinai. ............. 20

Figure 13. Stream density map in Km/Km$^2$ over the basement terrain of Southern Sinai. .......... 21

Figure 14. Slope map (in degrees) over the basement terrain of Southern Sinai.......................... 22

Figure 15. (A) Fault/Shear zone intersections over the study area. ............................................. 23

Figure 16. (A) Google map showing the five investigated wadies. ............................................. 24

Figure 17. Field photos were taken showing a 100-MHz antenna being pulled along each profile. ........................................................................................................................ 26

Figure 18. Sample raw GPR profiles (time in nS along the y-axis, and horizontal distance in m along the x-axis)........................................................................................................ 29

Figure 19. (a) Field image illustrates the components of the SYSCAL R2 resistivity imaging system. ....................................................................................................................... 31

Figure 20. Examples of raw resistivity data collected at the study area. .................................... 31

Figure 21. Summit X One system components. .......................................................................... 34

Figure 22. (a) The Summit X One 48-channel seismograph system in the field. ......................... 35

Figure 23. Examples of SR raw data quality from eight shot points (SP1, SP3, SP5, SP7, SP9, SP11, SP13, SP15) of seismic profile SR 1. .................................................................. 35

Figure 24. Location of drilled groundwater wells that we have recorded. .................................. 36

Figure 25. Examples of groundwater wells. ................................................................................ 37

Figure 26. Spatial distribution of potential recharge locations, as well as the productive groundwater wells. ........................................................................................................ 40

Figure 27. (A) Fault/Shear zone intersections as optimal locations for drilling groundwater wells and the regional groundwater flow direction (Abouelmagd et al., 2014; Mohamed et al., 2015).41

Figure 28. Modeled layer depth, thickness, and apparent resistivity, and the RMS values for 11 VESs collected in southern Sinai. ................................................................................. 45

Figure 29. Field pictures showing faults/shear zones and their intersections. ............................. 47

Figure 30. (A) Spatial variation in the resistivity, thickness, and depth to the saturated zone as indicated from interpretation of VESs data. .................................................................. 49

Figure 31. South-to-north geoelectric cross-section combining VES 4, VES3, VES 2, VES 5, VES 6, VES 11, VES 7, 8, and VES 9........................................................................................ 50

Figure 32. Travel time-distance plots showing three main layers. ............................................... 53

Figure 33. Seismic cross sections show three subsurface layers: unsaturated sediments (purple), saturated sediments (yellow), and basement rocks (blue). ........................................................... 55

Figure 34. (A) Spatial variation in the velocity, thickness, and depth to the saturated zone as indicated from interpretation of SR data........................................................................... 56

Figure 35. Processed GPR profiles (depth in m along the y-axis, and horizontal distance in m along the x-axis)........................................................................................................... 59

LIST OF TABLES

Page

Table 1. GPR profiles' locations, lengths, and directions........................................................... 27

Table 2. GPR data acquisition parameters. ..................................................................... 28

Table 3. GPR data processing steps and parameters..................................................... 28

Table 4. VES's acquisition locations and current electrode separation. ...................................... 30

Table 5. SR profiles' locations and lengths. ..................................................................... 33

Table 6. Seismic refraction data acquisition parameters. ............................................................ 34

Table 7. Locations of groundwater wells and their depth to water table (DTW). ........................ 36

Table 8. Seismic refraction studies with interpreted Vp values for saturation zones. Modified after (Azhar et al., 2019). ........................................................................................ 50

# 1. INTRODUCTION

## 1.1 Overview

Egypt occupies nearly one million square kilometers in the northeastern corner of Africa (Figure 1). It is bordered by the Mediterranean Sea on the north and the Red Sea on the east. Egypt is the third most populous country in Africa, with a population of over 107.9 million people (Egypt Population Live). Egypt has two types of freshwater resources: conventional and non-conventional. The Nile River, rainfall, and groundwater represent conventional water resources. Using wastewater and saltwater desalination are examples of non-conventional water supplies (Djuma et al., 2016).

Egypt, an arid country that relies on the Nile River as its primary water source, is experiencing water stress due to limited supplies, a growing population, and increased competition for water from countries in the upper Nile Basin. Climate change influences Nile discharge and can be viewed as a new challenge for Egypt's water resources. Since the 1990s, Egypt's primary challenge has been the rapidly expanding gap between limited water resources and escalating demand for that water (Abd Ellah, 2020).

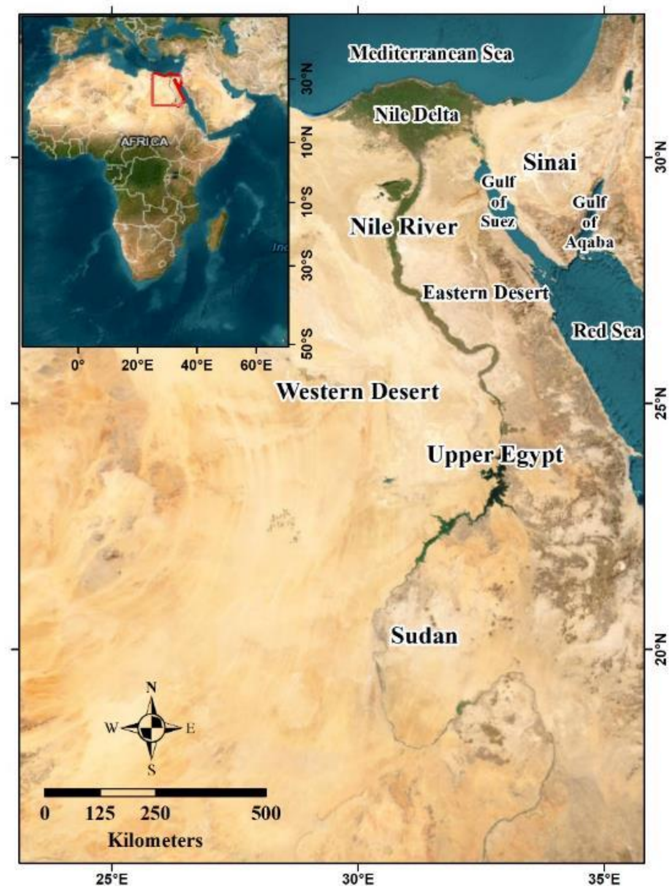


Figure 1: Location map showing Egypt's location and main physiographic features.

The Nile River is the second longest river in the world. In addition to Egypt, the Nile runs through or along the borders of 10 other African countries. Its three main tributaries are the White Nile, the Blue Nile, and the Atbara (Kameri et al., 2008). Because the Nile's water sources are located outside Egypt's borders, the river's land is highly vulnerable to changing climate conditions and is affected both within and without its borders. The impact of climate change on the Nile flow may cause floods and droughts in Egypt (Abd Ellah, 2020).

The majority of Egypt is classified as hyperarid, with very little rainfall (Awadallah et al., 2017). Egypt's climate zones are divided into seven zones (Hamed et al., 2022) (Figure 2). Zone 1 (Mediterranean) is located on Egypt's north coast, where the rainfall is the highest (118.3 mm), and the temperature is relatively low (25 °C), followed by Zone 2 (Nile Delta-1), a region that parallels the Mediterranean Sea, which receives the second-highest rainfall (58.1 mm) and the maximum temperature of 26.1 °C and the minimum temperature of 15.2 °C. Zones 3 (Nile Delta-2) and 7 (Sinai Mountains) have similar rainfall (19 mm); however, due to higher elevations, Zone 7 has lower maximum and minimum temperatures (24.4 and 11 °C, respectively) than Zone 3. Zone 4 (Middle Egypt) receives moderate amounts of annual rainfall (7.55 mm) with maximum and minimum temperatures of 29.13 and 15.54 °C, respectively. Because inland locations in southern Egypt, Zones 5 (Upper Egypt-1) and 6 (Upper Egypt-2) receive the least rainfall (2.19 and 1.76 mm, respectively) (Figure 2A).

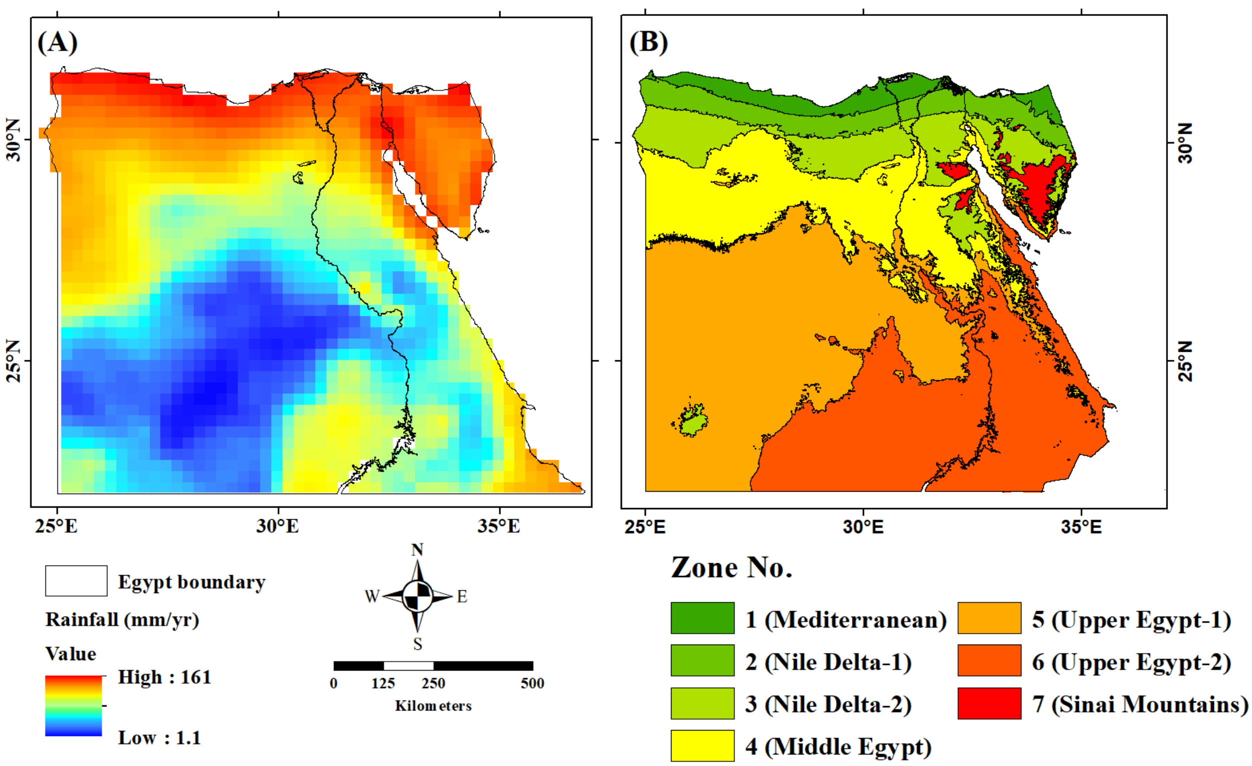


Figure 2: (A) Annual rainfall (mm/yr) over Egypt (Ahmed et al., 2022); (B) The seven climate zones of Egypt (Hamed et al., 2022).

Southern Sinai has a more temperate climate than the rest of Egypt's arid regions. Summer temperatures range from 23 to 32 °C, while winter temperatures range from 9 to 12 °C (JICA, 1999). The area is characterized by mostly orographic precipitation caused by forcing moist air masses to higher altitudes and condensation of their moisture as snow or rainfall in the form of flash floods. During rainy seasons, the relative humidity ranges from 30% to 60% and can reach 90% (El-Shamy et al., 1989).

Egypt is a pioneering country in the reuse of water since 1920. Four billion cubic meters of drainage water generated in the Delta's southern reaches are mixed with freshwater and reused for various purposes (Abdin & Gaafar, 2009). Desalination operations involve three main branches: seawater, groundwater, and wastewater. Egypt is also using seawater desalination as a water supply (Fried & Serio, 2012). Modern technological methods for seawater desalination are suggested in Egypt, as many sectors such as tourism, petroleum, urban coastal communities, and industry rely on this water resource.

Egypt's second freshwater source is groundwater, accounting for approximately 12% of the total water supply (Abo-El-Fadl, 2013). The impact on groundwater is directly related to the effects of climate change on recharge rates, which can fall in proportion to precipitation decreases and vice versa. Given its relatively high precipitation, the Sinai Peninsula (Figure 3) is one of Egypt's most promising regions for developing groundwater resources. In Sinai, rainfall is channeled as surface runoff through wadi networks and subsurface groundwater flow through wadi fill deposits and fractured basement rocks (Mohamed et al., 2015).

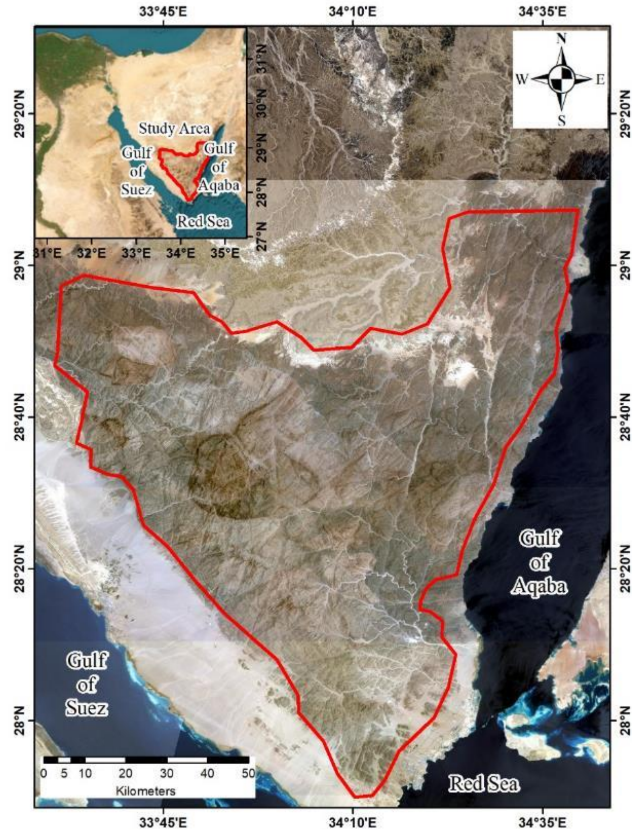


Figure 3: Location map of the study area (red polygon) in the Sinai Peninsula, Egypt.

### 1.2 Freshwater in Sinai

Current development plans in southern Sinai (population: $105 \times 10^3$) have increased stress on its limited and precious freshwater resources. In southern Sinai, freshwater comes mainly from small-scale desalination plants, piped Nile River water, and groundwater wells. Freshwater resources derived from desalination plants are too expensive for the indigenous people (Bedouin) to use to support their herding, agriculture, and cattle-raising activities. The pipeline project intended to transfer Nile water to southern Sinai is challenged by southern Sinai's higher elevation (>1,500 m above mean sea level), low injection volumes at the source station, and unresponsible practices of local farmers distributed along the pipeline path. Hence, groundwater resources in the basement terrains are the only feasible source of freshwater that can sustain the Bedouin communities in southern Sinai. However, the Bedouin community lacks a basic understanding of how these resources are developed, recharged, distributed, and protected and how to use them sustainably.

### 1.3 Challenges

Few studies have been conducted on groundwater exploration in the basement terrain of southern Sinai. These studies were limited to specific areas. Some used remote sensing or geophysical data, while others combined remote sensing and geophysical data. None of these studies investigated the full controls of structural elements on groundwater accumulation and flow in the whole basement terrains of the Sinai Peninsula (Figure 3).

Issar and Gilad, (1982) reported three main groundwater flow systems in Southern Sinai: along the regional crustal fractures parallel to the Gulf of Elat Rift, in shallow fractured rocks, and wadi beds that is governed by the dike system. They found that recharge into fractured crystalline aquifers and interconnected gravel bed aquifers is 10-15% of total precipitation. Their research focused on the use of remote sensing data and was not fully confirmed with field investigations.

Shendi and Elrayes (1992) used three geophysical techniques (magnetic, geoelectric, and seismic refraction) to prospect for groundwater in the basement terrain of Wadi Isbaeya and Wadi Elsheikh in southern Sinai. Their results defined two sites in Wadi Elsheikh for drilling groundwater wells at depths up to 40 m. Their study was restricted only to these locations. In addition, Zayed, (2021) used geoelectrical resistivity sounding to investigate groundwater in Wadi Morra, southern Sinai. His results were also limited to a local region. Similarly, Arnous (2016) delineated, identified, modeled, and mapped groundwater potential zones in southern Sinai using remote sensing data and GIS. His findings were limited to smaller geographic extent and focused on local-scale groundwater potential mapping within the Ferian watershed.

Mohamed et al., (2015) used integrated approach (very low frequency electromagnetic, magnetic, remote sensing, and geographic information system [GIS]) to investigate the structural controls on the groundwater flow in Ferian watershed, southern Sinai. They found that the distribution of the water-bearing features corresponds to that of fractures, faults, shear zones, dike swarms, and wadi networks. The orientations of these fractures relative to the groundwater flow affect the groundwater accumulation. For example, the NW-SE to N-S trending conductive features that intersect the groundwater flow (SE to NW) at low angles capture groundwater flow, whereas the NE-SW to E-W features that intersect the flow at high angles impound groundwater upstream and could provide potential productive well locations. However, it is important to note that the conclusions drawn regarding the structural controls on groundwater flow in their study were primarily based on the distribution of a limited number of wells rather than extensive geophysical campaigns. While the well data served as a useful indicator of groundwater behavior, it is acknowledged that a more comprehensive understanding could be achieved through conducting intensive geophysical campaigns. These campaigns would involve employing a wider range of geophysical techniques to obtain more detailed information on subsurface structures and hydrogeological characteristics. By integrating the findings from such intensive geophysical campaigns with the existing well data, a more robust understanding of the structural controls on groundwater flow could be established.

### 1.4 Objective

Southern Sinai is a mountainous area (up to 2,625 m above sea level) covered entirely by igneous basement granitic and volcanic rocks (Figure 3). Several geologic structures (e.g., faults, dikes, and joints) highly affect these rock units with different distributions, attitudes, and densities. The geologic structures control the spatial distribution of ephemeral valleys in the Southern Sinai area. These wadies are covered with alluvial deposits (e.g., gravels, sands) of varying thicknesses. Groundwater is either residing in these alluvial deposits (e.g., alluvial aquifers) or the fractured basement (fracture basement aquifers). The main goals of this research are to (1) map potential recharge and extraction locations for these aquifers, and (2) investigate the structural controls on groundwater accumulation and flow (e.g., pathways or barriers) in these aquifers.

### 1.5 Significance

A comprehensive understanding of locations, mechanisms, and characteristics of structural elements concerning groundwater accumulation and flow could improve our understanding of hydrogeological processes within the basement aquifers, enhance groundwater exploration activities, improve groundwater management practices, and increase the efficiency and cost-effectiveness of drilling operations. The results of this research could guide future geophysical data collection activities and help select potential locations for groundwater wells, thus reducing field time, effort, and resources. Also, this research compares the results of three geophysical techniques in mapping groundwater resources in basement terrains, thus enabling a better understanding of the limitations and advantages of each technique.

## 2. STUDY AREA

### 2.1 Overview

This research was conducted in southern Sinai, Egypt. The study area is bordered by the Red Sea on the south, the Gulf of Aqaba on the east, and the Gulf of Suez on the west (Figure 3). This chapter covers the geologic, structural, and hydrogeologic setting of the study area.

### 2.2 Geologic and Structural Settings

Southern Sinai is a mountainous area (Figure 4) covered entirely by igneous basement granitic and volcanic rocks (Figure 5). Examples of rock units in the Southern Sinai include granites, granodiorites, monzonites, and syenites (El-Shafei & Kusky, 2003; Kabesh et al., 2013). Outcrops cover approximately 70% of Southern Sinai (Mohamed et al., 2015).

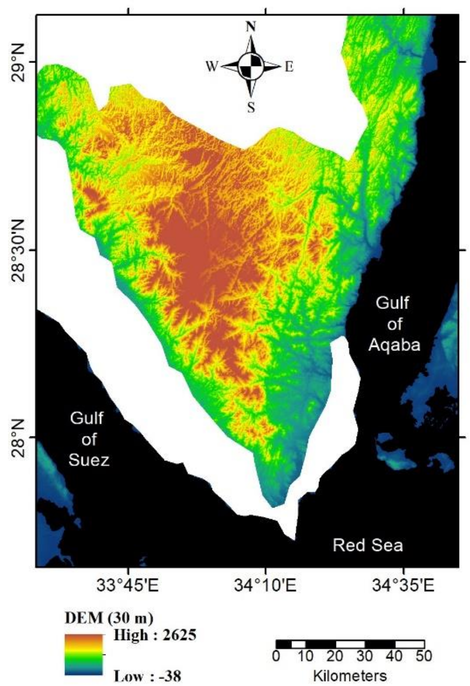


Figure 4: Topographic map of southern Sinai.

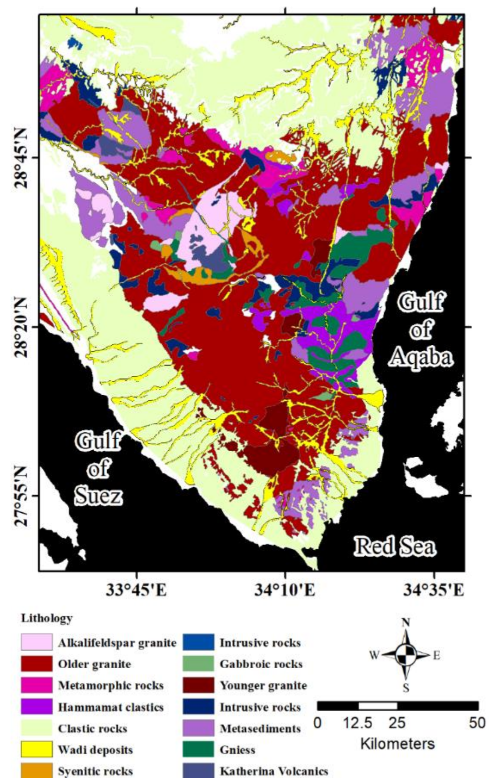


Figure 5: Simplified geologic map of the study area (modified from Conoco, 1987).

Southern Sinai is structurally influenced by the Red Sea rifting, the Gulf of Suez (NW-SE trend), and the Gulf of Aqaba (NNE-SSW trend), all of which formed several structural elements (e.g., faults, shear zones, dikes; Figure 6) during their development (Sharp et al., 2000). The geologic structures control the spatial distribution of ephemeral valleys (also called wadies) in the Southern Sinai (El-Sayed, 2006). These wadies are covered with alluvial deposits (e.g., gravels, sands) of varying thicknesses (30–100 m). In addition, the structural elements significantly affected groundwater accumulation and flow in southern Sinai (Babiker & Gudmundsson, 2004; Gudmundsson, 2000; Issar & Gilad, 1982).

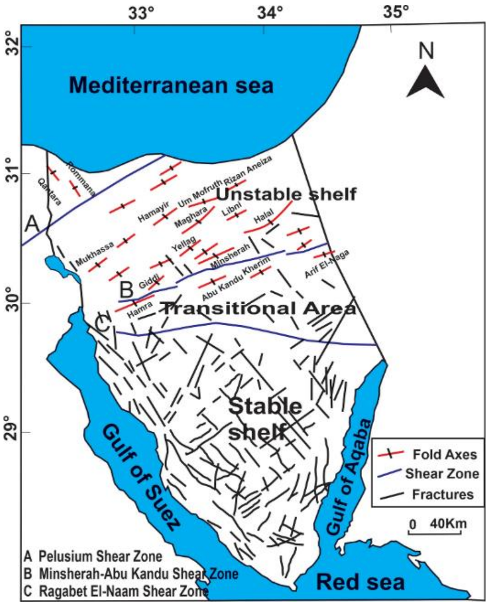


Figure 6: Structural map showing the main structural elements in Sinai (Gaber et al., 2022; Neev, 1975).

### 2.3 Hydrogeologic Setting

In southern Sinai, orographic effects control precipitation; moist air masses are forced to higher altitudes where condensation occurs, resulting in rainfall or snow deposition (Figure 2A). The dense valley networks (Figure 7) collect precipitation over large areas and channel it downstream through the main valleys, causing flash floods (Mohamed et al., 2015). Rainfall is transported downstream as a combination of surface runoff in valley networks and as groundwater flow in the alluvial sediments beneath these valleys, in the fractured basement, and down-dropped sedimentary units within the basement complex (Amer et al., 2013; Sultan et al., 2007, 2008, 2011). The average annual precipitation over the study area is estimated at 50 mm, with surface runoff estimated to be 14 x $10^6$ $m^3$/yr and a net groundwater recharge at 11 x $10^6$ $m^3$ (Elewa & Qaddah, 2011).

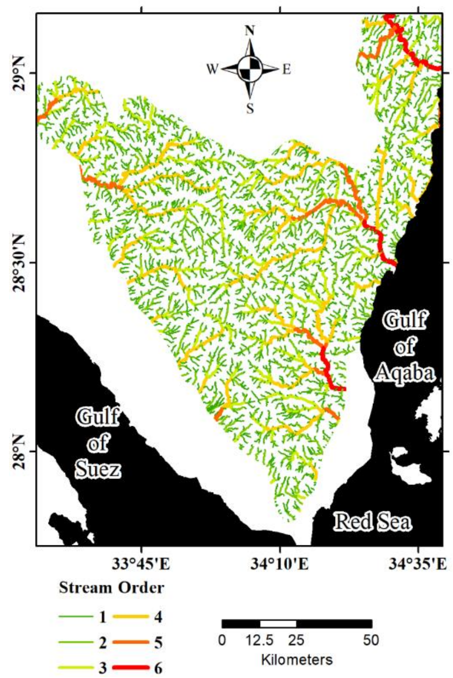


Figure 7: Stream network over the study area.

Two main types of aquifer systems in the Southern Sinai include weathered/fractured basement aquifers and alluvial aquifers (Figure 8) (Shendi & Abouelmagd, 2004). The Precambrian fractured basement aquifers are composed of metamorphic and igneous rocks that have been weathered and fractured over time (Figure 8). Given the thin weathered zone and higher gradient, this aquifer has a relatively low yield, particularly in the upstream areas. Recharge to this aquifer mainly depends on direct precipitation that percolates through the fracture systems (Mohamed et al., 2015). The water table in the fractured basement aquifer is relatively shallow (2–8 m) (El-Rayes, 1992; Shendi & Abouelmagd, 2004). The alluvial aquifer is represented by the Quaternary terraces and wadi filling deposits (e.g., sand and gravel). This is an unconfined aquifer with fair to good productivity and a thickness between 3 and 150 m. In the Southern Sinai, the alluvial aquifer rests unconformably on the Precambrian solid or weathered/fractured basement igneous and metamorphic rocks. The maximum thickness of the Quaternary aquifer is usually aligned with the wadi main axis (Figure 8). The depth to the water table in the alluvial aquifer ranges from 2 to 47 m (Abouelmagd, 2003).

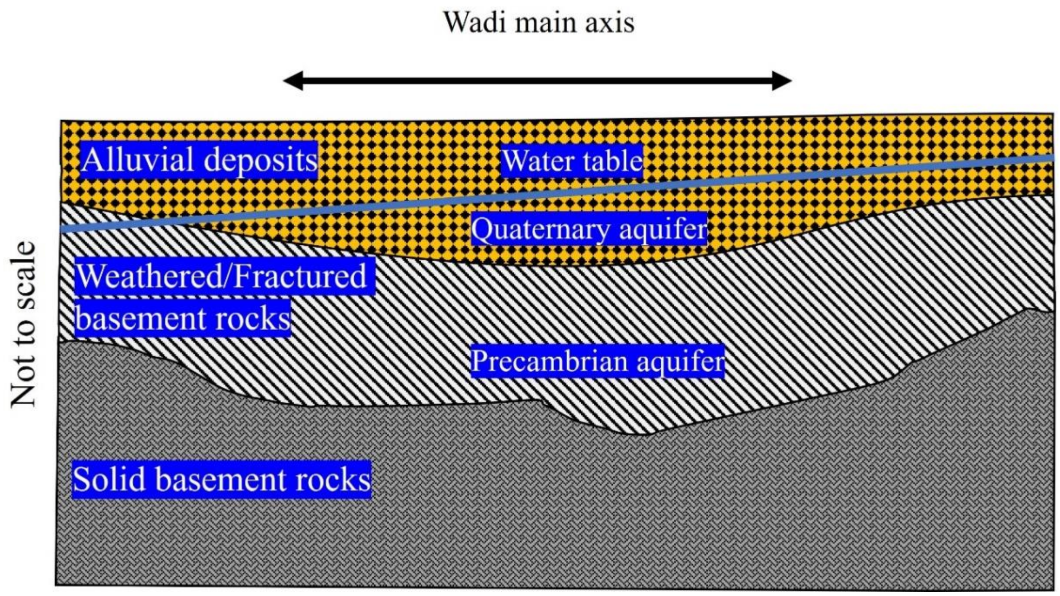


Figure 8: Schematic showing aquifer types and geometries within Southern Sinai's main wadies. The blue-gray line is the top of water saturation zone.

# 3. DATA AND METHODS

## 3.1 Overview

An integrated approach that combines remote sensing data, field geophysical measurements, and geographic information system (GIS) techniques was used in this study. The ultimate goal was to characterize the optimal locations for groundwater recharge and extraction and examine how they are affected by geologic structures. Initially, remote sensing data and GIS techniques were used to (1) model optimal recharge areas, and (2) define optimal locations for drilling sustainable groundwater wells (e.g., optimal groundwater extraction location). Field geophysical surveys were then acquired to validate optimal extraction locations. An integrated geophysical approach that combines vertical electrical sounding (VES), seismic refraction (SR), and ground penetrating radar (GPR) was used.

## 3.2 Remote Sensing Data and GIS Techniques

### 3.2.1 Weighted Overlay Model (WOM)

In this study, the Weighted Overlay Model (WOM) was used to map potential recharge locations in Southern Sinai. This model applies overlay analysis to solve multicriteria problems (Nasir et al., 2018). This model has been extensively used to create precise groundwater potential maps for many regions across the globe (Fatema et al., 2023; Arulbalaji et al., 2019; Faheem et al., 2023; Karimi et al., 2022; Mandal et al., 2021; Nasir et al., 2021; Zimik et al., 2022).

The WOM is mathematically represented by:

$$\mathrm{Recharge} = \sum_{\mathrm{i}=1}^{\mathrm{n}} \mathrm{W_i}\, \mathrm{X_i}$$

where $\mathrm{W_i}$ indicates the normalized weight of each input layer, $\mathrm{X_i}$ is model input layers, and $\mathrm{n}$ is the number of input layers.

Six input data layers were used as model inputs: surface lithology, rainfall, slope, stream density, fault density, and fault intersection. These layers are known to have a significant impact on recharge rates. For example, recharge rates are expected to be higher in areas with higher rainfall rates, fault densities, stream densities, lower slopes, and porous lithology (Kaewdum & Chotpantarat, 2021). The input layers were normalized between 0 and 1 to account for varying units and ranges using the following equation:

$$\hat{X}_i = \frac{X_i - X_{min}}{X_{max} - X_{min}}$$

where $\hat{X}_i$ is the normalized value for $X_i$ and $X_{min}$ and $X_{max}$ are the minimum and maximum values for the time series.

### 3.2.2 Model Input Data

#### i. Rainfall

The average annual rainfall data (Figure 9) were extracted from the Integrated Multi-satellite Retrievals for Global Precipitation Measurement (IMERG) product of the Global Precipitation Measurement (GPM) mission, which provides half-hourly and monthly precipitation products on a 0.1° × 0.1° grid scale over the globe (Huffman et al., 2019). IMERG merges and interpolates satellite precipitation with rain gauge estimates to produce high-resolution rainfall products. Compared to other remote-sensing-derived rainfall products, GPM provides better accuracy and improved sampling (Hou et al., 2014). It can also capture the intermittency of precipitation in most climatic and hydrologic zones (Shen & Xiong, 2016).

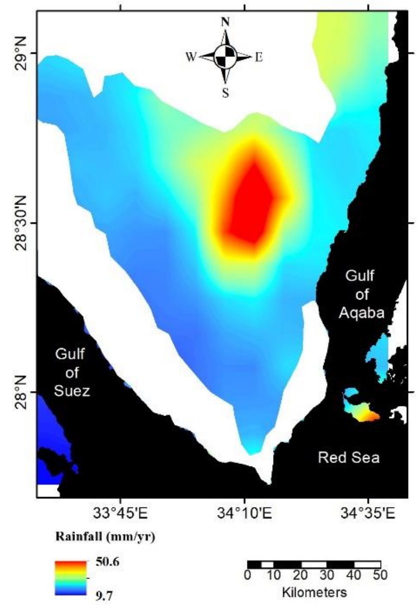


Figure 9: Average annual rainfall data over the basement terrain of Southern Sinai.

### ii. Surface Lithology

The surface lithology (Figure 10B) was digitized from the available geologic maps (Figure 5) and remote-sensing data (Figures 10A and 10B). Three Landsat Thematic Mapper (TM) scenes (ID: LT51740402011116MTI00, LT51750402011203MTI00, and LT51740412011244MTI00) were used to generate false-color ratio composites over southern Sinai (Figure 10A). These ratio images (blue: 5/4 × 3/4, green: 5/1, and red: 5/7) are sensitive to rock content of iron-bearing aluminosilicates, spectrally opaque, and hydroxyl-bearing or carbonate-bearing minerals, respectively (Sultan et al., 1987). Rock units rich in hydroxyl-bearing minerals and spectrally opaque phases appear red; rocks rich in iron-bearing aluminosilicates (e.g., amphibolites, gabbros, and mafic volcanic) appear blue; and rocks poor in iron-bearing aluminosilicates, hydroxyl-bearing minerals, and opaque phases (e.g., granites) appear green. Higher weights were assigned to highly fractured rock units within the surface lithology layers because they have high infiltration capacity.

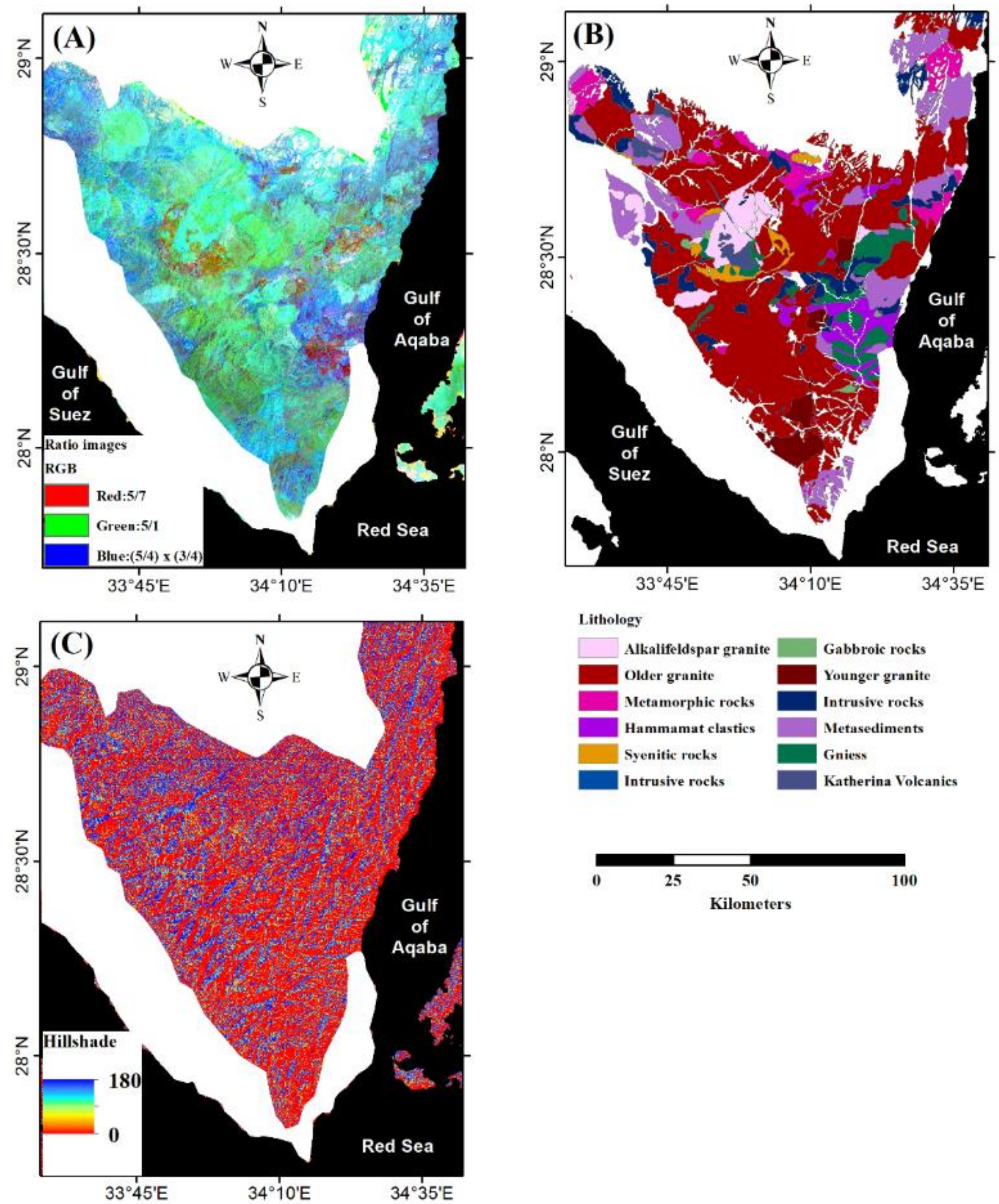


Figure 10: (A) Landsat TM band ratio color composite image (5/7: red; 5/1: green; 5/4 x 3/4: blue) over the study area; (B) Simplified geologic map (modified after Conoco, 1987); and (C) Hillshade map over the basement terrain of Southern Sinai.

### iii. Geologic Structures

Geologic structures (faults and shear zones) (Figure 11) were mapped from ratio images (Figure 10A), geologic maps (Figure 10B), and Hillshade map (Figure 10C). The following criteria were used to identify the distribution of faults and shear zones from the Landsat and ratio images (Mohamed et al., 2015; Sultan et al., 2000): (a) the presence of lithologic linear discontinuities that are tens (faults) to hundreds of meters (shear zones) wide; (b) presence of subparallel topographic ridges within the shear zones, which are probably caused by differential weathering of lithologic units within shear zones, units that are compositionally different; and (c) lateral displacement and/or reorientation of outcrop patterns of distinctive lithologies and structural trends to align with inferred faults or shear zones in the case of strike-slip displacements. Linear features with high contrast in Hillshade that show significant displacements and offsets were used to define geologic structures in the study area (Figure 10C). The generated faults/Shear zones were validated using visible Google Earth images (Figures 11C and 11D). The fault density layer was generated using the kernel density function in a GIS environment (Figure 12).

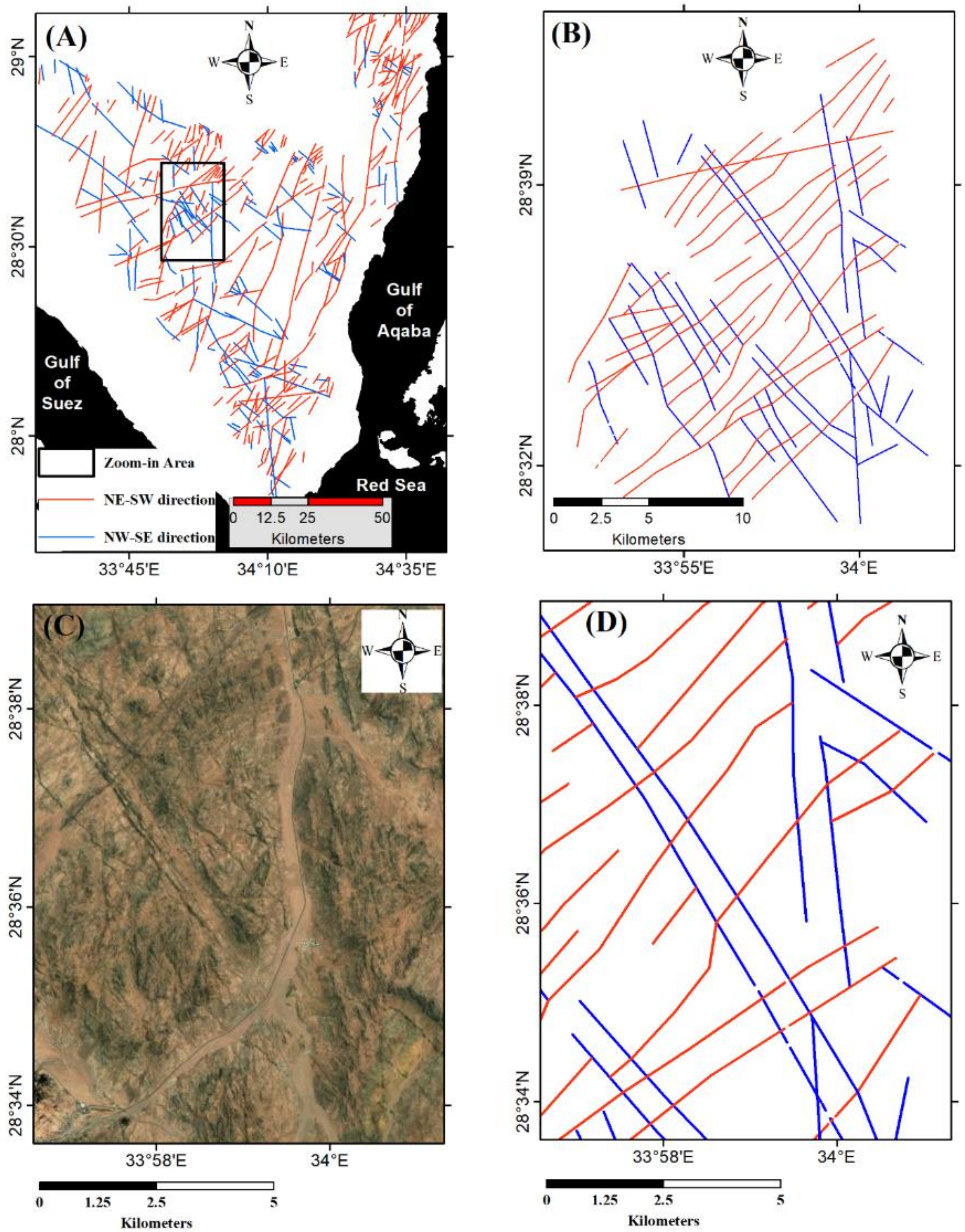


Figure 11: (A) Spatial distributions of faults and shear zones over the basement terrain of Southern Sinai; (B) Zoomed-in for better visualization showing faults and shear zones; (C) High-resolution Google Earth image; and (D) Spatial distributions of faults and shear zones for area shown in panel C.

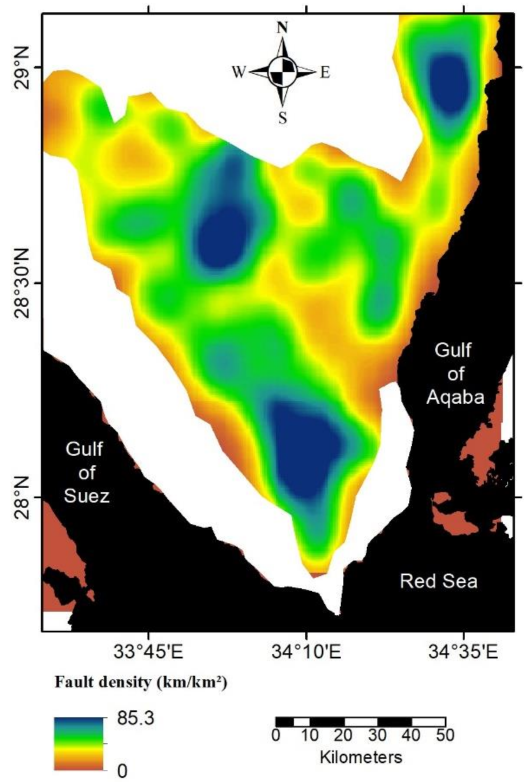


Figure 12: Fault density map in Km/Km$^2$ over the basement terrain of Southern Sinai.

**iv. Stream Network**

Stream networks (Figure 7) were derived from DEM data (Drisya, 2016). The southern Sinai's DEM was extracted from publicly available Shuttle Radar Topography Mission (SRTM) data with 30-m spatial resolution (Figure 4). Stream network was extracted in a GIS environment using a number of geoprocessing tools. First, sinks are filled to create a depression-free DEM; second, flow directions are determined; and third, flow accumulation is calculated as the sum of the flow accumulation values of the neighboring cells into which the flow is directed (Cooper, 2010). Stream density was generated using the kernel density function in a GIS environment (Figure 13).

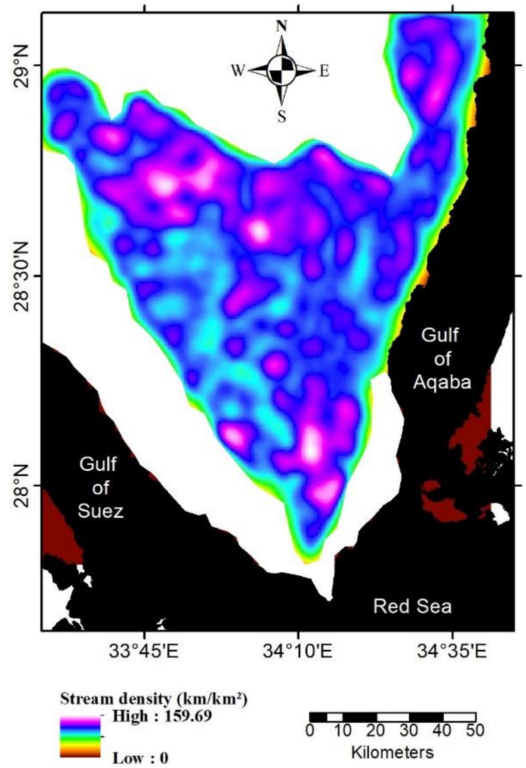


Figure 13: Stream density map in Km/Km$^2$ over the basement terrain of Southern Sinai.

### v. Slope

The slope image (Figure 14) was created from the DEM data in a GIS environment (Paz & Collischonn, 2007). The slope product expresses the change in elevation over a given distance.

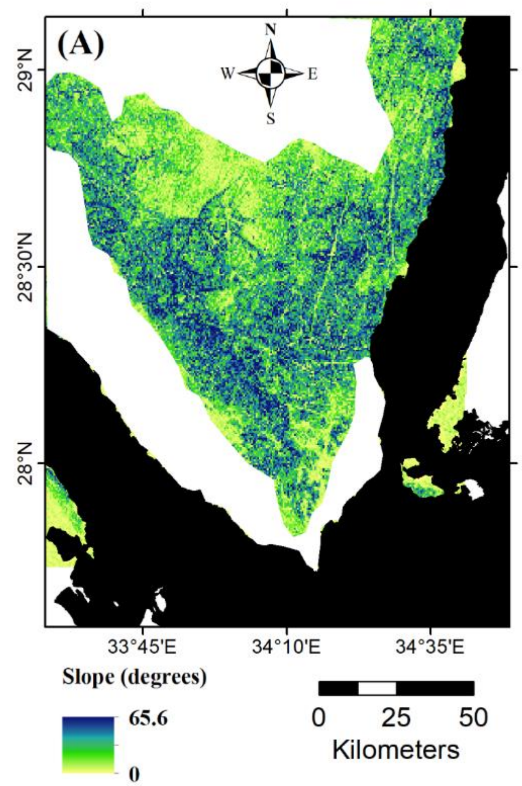


Figure 14: Slope map (in degrees) over the basement terrain of Southern Sinai.

### 3.2.3 Optimal Locations for Drilling Sustainable Groundwater Wells

Locations of sustainable groundwater wells (Figure 15) were mapped at the intersections of (1) two or more fault systems and (2) a shear zone and a fault system. These intersections increase porosity and create favorable conditions for groundwater to be accumulated within the basement and alluvial aquifer systems (Blenkinsop & Kadzviti, 2006; Goddard & Evans, 1995; Mohamed et al., 2015). When faults/shear zones intersect or cross each other, they create zones of increased fracture density and complexity. These intersections are characterized by increased fracture conductivity, enhanced recharge rates, high potential to capture and store of groundwater, and increased water-bearing capacity (Mohamed et al., 2015). These locations were mapped in the GIS environment. These locations were then confirmed using different field geophysical measurements.

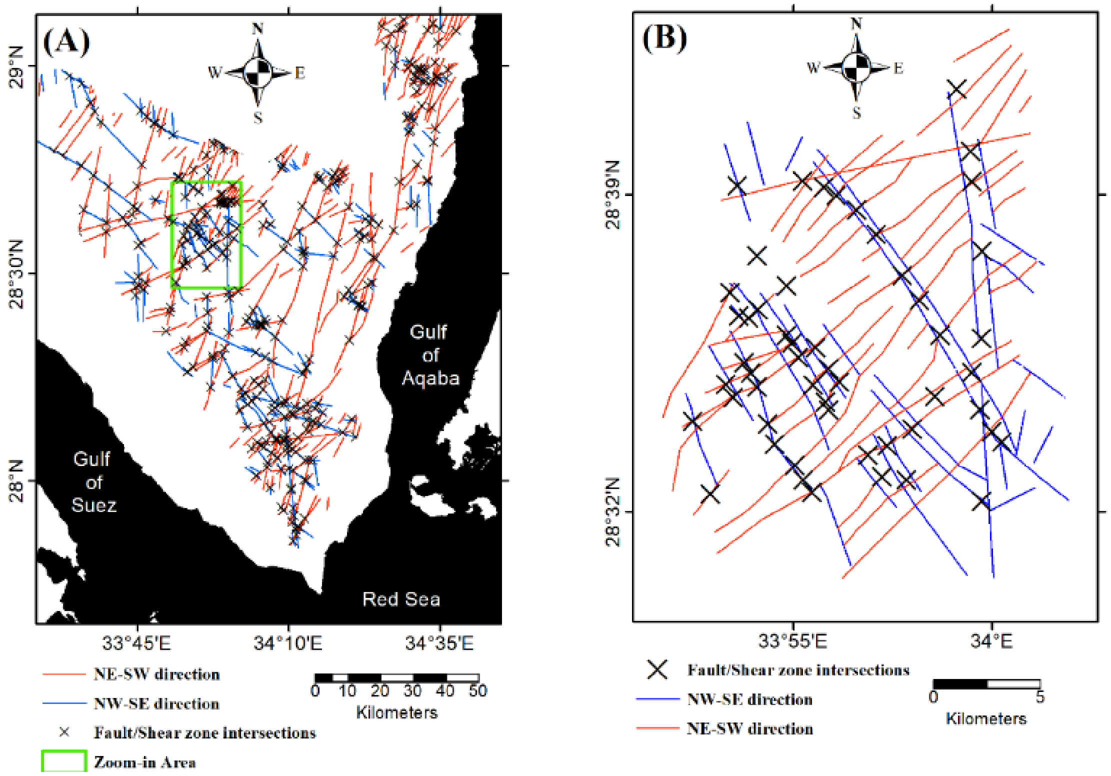


Figure 15: (A) Fault/Shear zone intersections over the study area; (B) Intersections over a zoomed area that has been used for geophysical investigations.

### 3.3 Near-surface Geophysical Techniques (Fieldwork)

In this study, three geophysical methods were used: ground penetrating radar (GPR), seismic refraction (SR), and vertical electrical sounding (VES) to validate, calibrate, and confirm optimal extraction locations (Section 3.2.3). Field work was conducted in five wadies (Elsheikh, Elfuria, Sudud, Isbaeya, and Ghreaba) (Figure 16). A detailed description of each of the geophysical methods is provided below.

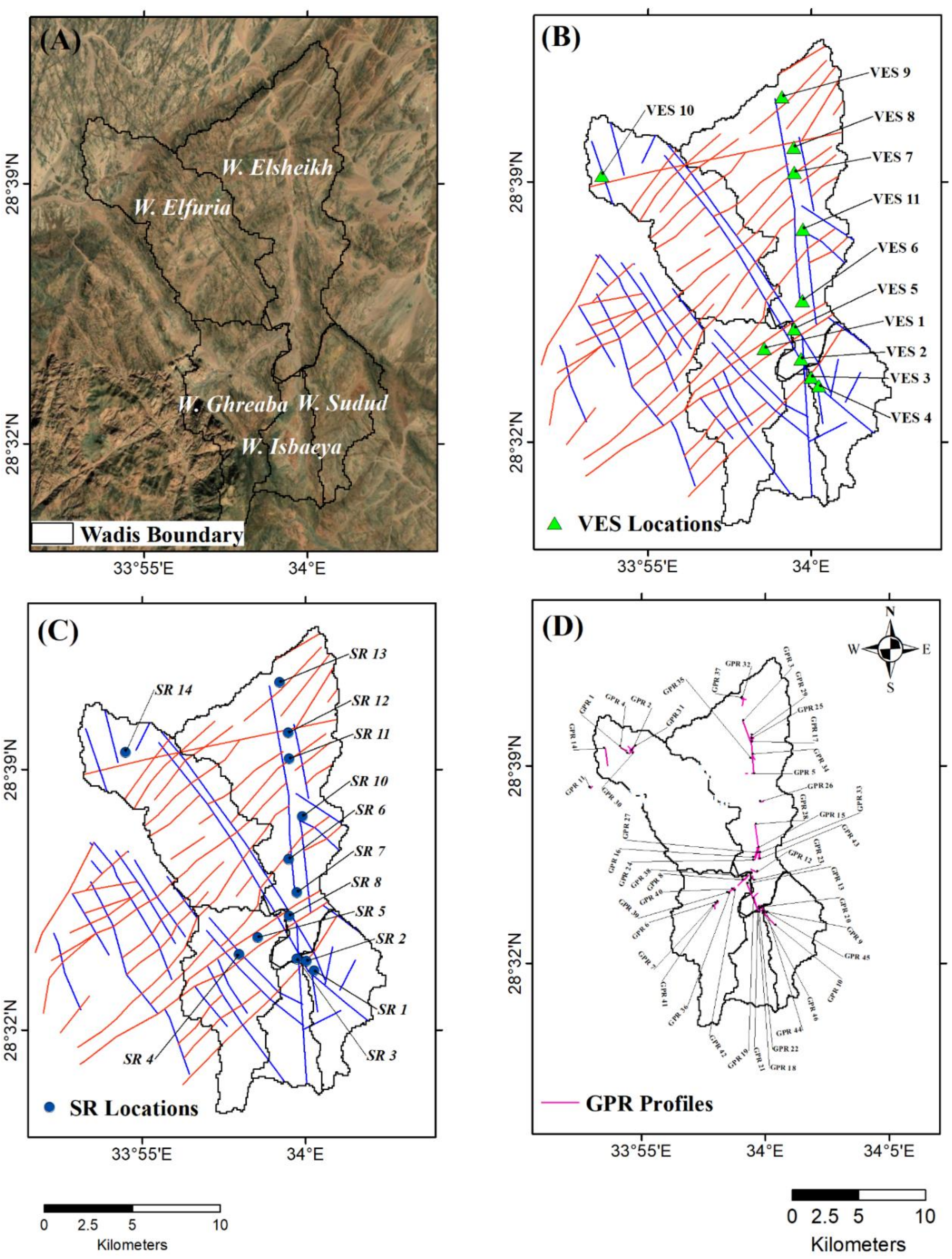


Figure 16: (A) Google map showing the five investigated wadies; (B) Location map showing the VES sites; (C) Location map showing the SR locations; and (D) Location map showing the GPR locations.

### 3.3.1 Ground Penetrating Radar (GPR)

GPR is a noninvasive geophysical tool specifically designed to penetrate underground materials and provide images of the shallow (0-30 m) subsurface (Doolittle et al., 2006). GPR operates by transmitting radio-frequency electromagnetic energy pulses into the subsurface. These electromagnetic energy waves travel through the soil until they interact with a layer or object with contrasting dielectric properties. Dielectric property contrasts cause some of the transmitted electromagnetic energy to be reflected back to the receiver antenna. The amount of energy an interface reflects is determined by the difference between the two layers' electric conductivity, relative dielectric permittivity, and relative magnetic permeability (Doolittle et al., 2006; Davis & Annan, 1989; Dam & Schlager, 2000).

GPR is a system that operates on a time scale. The system measures the time it takes electromagnetic energy to travel from an antenna to an interface (e.g., water table, soil horizon, stratigraphic layer) and back. GPR typically yields a time-distance record of the subsurface. The horizontal scale is a distance scale based on the speed with which the antenna moves across the ground surface. The vertical scale represents the radar pulse's two-way travel time through the subsurface. GPR has been successfully used for groundwater investigations in arid and semi-arid environments (Amer et al., 2013; Essam et al., 2020; Mahmoudzadeh et al., 2012).

In this study, GPR profiles were acquired using GSSI’s SIR-3000 GPR system and a 100-MHz antenna (Figure 17). GPR profiles (total: 46; length: 50–2440 m) were collected along locations parallel and perpendicular to the main axis of each of the investigated wadies (Table 1).


Figure 17: Field photos were taken showing a 100-MHz antenna being pulled along each profile. The GPR profiles were recorded and stored on the GSSI's SIR-3000 control/display unit, which the operator carried as the antenna moved. The top left image also depicts a productive well located in that area.

Table 1: GPR profiles' locations, lengths, and directions.

| Wadi Name | Profile Name | Start point | | End point | | Length (m) | Direction to the Wadi (Perpendicular⊥ /Parallel //) |
|---|---|---|---|---|---|---|---|
| | | Longitude (degree) | Latitude (degree) | Longitude (degree) | Latitude (degree) | | |
| **Sudud** | GPR 1 | 34.0062 | 28.5564 | 34.00623 | 28.55645 | 50 | ⊥ |
| | GPR 2 | 34.00613 | 28.55626 | 33.9978 | 28.56452 | 1224 | // |
| | GPR 30 | 34.00145 | 28.56427 | 34.00062 | 28.56413 | 85 | ⊥ |
| | GPR 31 | 34.00062 | 28.56413 | 33.99842 | 28.56425 | 217 | ⊥ |
| **Isbaeya** | GPR 25 | 33.99786 | 28.56681 | 33.99936 | 28.56228 | 523 | // |
| | GPR 27 | 33.99475 | 28.56464 | 33.99794 | 28.56453 | 308 | ⊥ |
| | GPR 32 | 33.99855 | 28.56385 | 33.99782 | 28.56603 | 251 | // |
| **Ghreaba** | GPR 12 | 33.9681 | 28.5689 | 33.96706 | 28.56986 | 154 | ⊥ |
| | GPR 13 | 33.9661 | 28.5682 | 33.96852 | 28.57035 | 338 | // |
| | GPR 15 | 33.9858 | 28.5828 | 33.98899 | 28.58593 | 467 | // |
| | GPR 18 | 33.97547 | 28.57503 | 33.97603 | 28.57561 | 85 | // |
| | GPR 19 | 33.97622 | 28.57511 | 33.97553 | 28.57567 | 92 | ⊥ |
| | GPR 20 | 33.97511 | 28.57572 | 33.97872 | 28.57753 | 405 | // |
| | GPR 21 | 33.97967 | 28.57717 | 33.97869 | 28.57842 | 169 | ⊥ |
| | GPR 22 | 33.98136 | 28.57936 | 33.98806 | 28.58517 | 918 | // |
| | GPR 46 | 33.96565 | 28.56807 | 33.96587 | 28.56559 | 270 | ⊥ |
| **Elfuria** | GPR 6 | 33.9099 | 28.6589 | 33.90811 | 28.65955 | 194 | ⊥ |
| | GPR 7 | 33.9069 | 28.6589 | 33.90237 | 28.6608 | 485 | // |
| | GPR 8 | 33.9114 | 28.6615 | 33.90807 | 28.65696 | 603 | // |
| | GPR 9 | 33.8924 | 28.6606 | 33.89374 | 28.64997 | 1280 | // |
| | GPR 10 | 33.8821 | 28.6367 | 33.88368 | 28.63817 | 220 | // |
| | GPR 44 | 33.90808 | 28.65703 | 33.912 | 28.6615 | 626 | // |
| | GPR 45 | 33.91156 | 28.65808 | 33.90733 | 28.66183 | 586 | ⊥ |
| **Elsheikh** | GPR 3 | 33.99275 | 28.59597 | 33.99476 | 28.60163 | 657 | // |
| | GPR 4 | 33.99496 | 28.60171 | 33.9938 | 28.60175 | 113 | ⊥ |
| | GPR 5 | 33.9902 | 28.6636 | 33-98472 | 28.67648 | 1523 | // |
| | GPR 11 | 33.9941 | 28.5873 | 33.98999 | 28.58901 | 447 | ⊥ |
| | GPR 14 | 33.9945 | 28.5658 | 33.98698 | 28.58125 | 1860 | // |
| | GPR 16 | 33.9866 | 28.6454 | 33.99172 | 28.64552 | 497 | ⊥ |
| | GPR 17 | 33.9920 | 28.6460 | 33.99002 | 28.66764 | 2440 | // |
| | GPR 23 | 33.99272 | 28.59447 | 33.99531 | 28.60075 | 740 | // |
| | GPR 24 | 33.99531 | 28.60075 | 33.99289 | 28.61556 | 1658 | // |
| | GPR 26 | 33.99508 | 28.57525 | 33.99203 | 28.57272 | 409 | ⊥ |
| | GPR 28 | 33.99481 | 28.56467 | 33.99203 | 28.57272 | 929 | // |
| | GPR 29 | 33.99718 | 28.56767 | 33.9955 | 28.56767 | 164 | ⊥ |
| | GPR 33 | 33.99567 | 28.59489 | 33.99486 | 28.59593 | 141 | // |
| | GPR 34 | 33.99594 | 28.5955 | 33.99584 | 28.59868 | 352 | // |
| | GPR 35 | 33.99584 | 28.59868 | 33.99543 | 28.59521 | 386 | // |
| | GPR 36 | 33.9918 | 28.58258 | 33.99099 | 28.5855 | 325 | // |
| | GPR 37 | 33.99907 | 28.62901 | 33.99591 | 28.62889 | 309 | // |
| | GPR 38 | 33.99253 | 28.66641 | 33.99024 | 28.66603 | 224 | ⊥ |
| | GPR 39 | 33.99152 | 28.66494 | 33.99038 | 28.66777 | 325 | // |
| | GPR 40 | 33.98742 | 28.68925 | 33.98394 | 28.68942 | 332 | // |
| | GPR 41 | 33.98517 | 28.69039 | 33.98428 | 28.68544 | 555 | // |
| | GPR 42 | 33.99222 | 28.65511 | 33.99078 | 28.65414 | 178 | ⊥ |
| | GPR 43 | 33.99294 | 28.6535 | 33.99081 | 28.65706 | 444 | // |

Time mode GPR survey was utilized. The samples per scan, scan rate, scans per meter, acquisition gains, and acquisition filters were adjusted through the initial tests. Table 2 lists the main GPR data acquisition parameters.

Table 2: GPR data acquisition parameters.

| Parameter | Value |
|---|---|
| **GPR system** | GSSI's SIR-3000 |
| **GPR antenna** | Monostatic 100 MHz |
| **Record range** | 500 ns |
| **Acquisition mode** | Time |
| **Scan rate** | 24 scans/second |
| **Sample rate** | 512 samples/trace |
| **Sample resolution** | 16 bits/sample |
| **Mark rate** | 30 sec |
| **Dielectric constant** | 2.5 to 5 |
| **Vertical filter** | High pass: 25 MHz; Low pass: 300 MHz |
| **Gain** | Automatic |

The collected GPR data were then processed and enhanced using the commercial Geophysical Survey Systems, Inc (GSSI) RADAN 7 software. Figure 18 shows sample raw GPR profiles. The processing steps included header editing, marks editing, distance normalization, horizontal filters (e.g., background removal and stacking), vertical filter (e.g., FIR), and gain adjustment. Table 3 lists the main processing steps applied for each of the collected GPR profiles.

Table 3: GPR data processing steps and parameters.

| Parameter | Value |
|---|---|
| **Header editing** | Scans/unit: (avg 17); unit/mark: (avg 32) |
| **Marks editing** | Add or edit user field marks |
| **Horizontal filters** | Stacking: Avg 39 traces; Background removal: avg 888 scans |
| **Vertical filter** | High pass: avg 35 MHz; Low pass: avg 114 MHz |

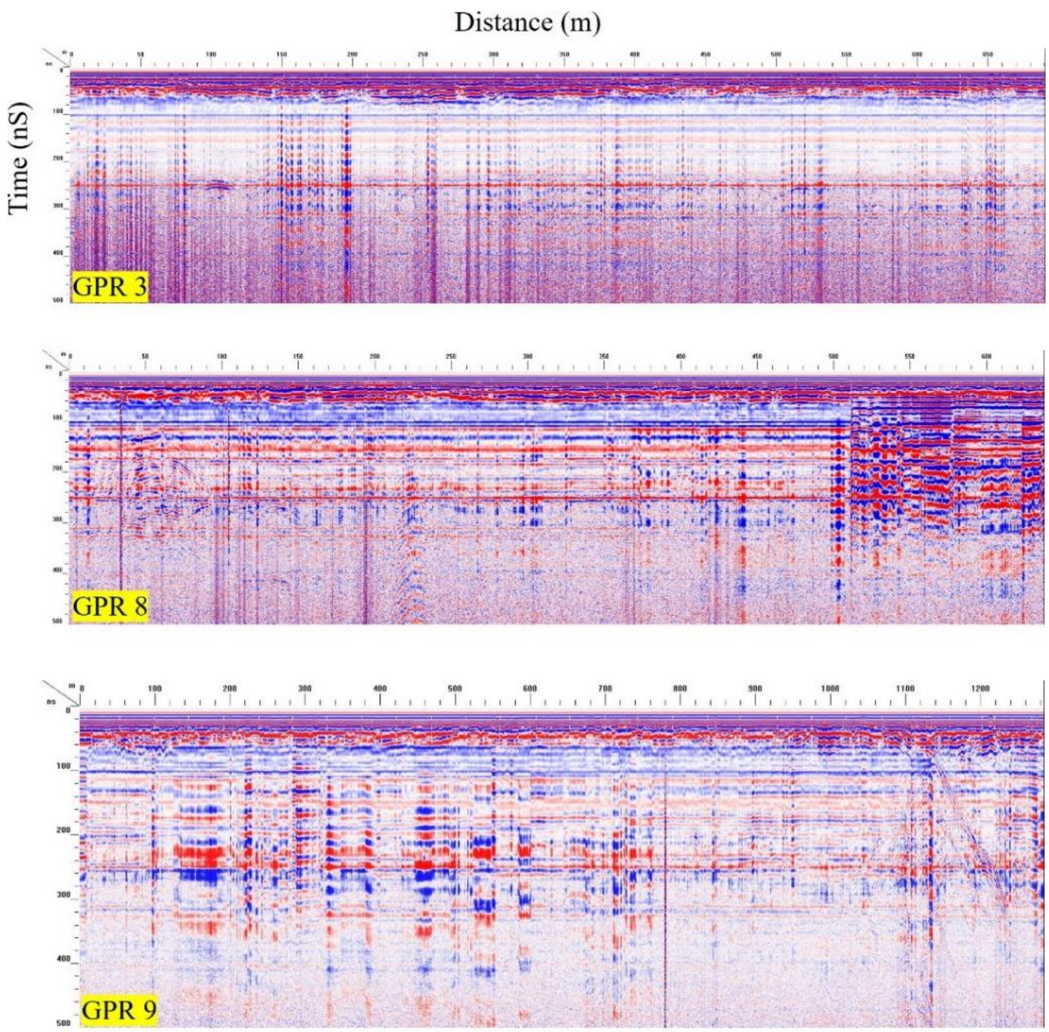


Figure 18: Sample raw GPR profiles (time in nS along the y-axis, and horizontal distance in m along the x-axis).

### 3.2.4 Vertical Electrical Sounding (VES)

The VES technique is commonly used for groundwater exploration to detect the vertical distribution of electrical resistivities and thicknesses of different lithologic units (Urish & Frohlich, 1990). This technique works well when the resistivities are different. Even when there is no groundwater, the electrical resistivity of alluvial deposits and the underlying basement terrain differ significantly. VES have been successfully used in hydrogeologic investigations in arid and semi-arid environments (Araffa et al., 2017; Genedi & Youssef, 2023; Mohamaden et al., 2016; Shendi & Abouelmagd, 2004).

There is only one way to inject a direct current into the ground: through a pair of electrodes connected to a primary potential source (DC generator, batteries, etc.). The electrodes, known as current electrodes, make direct galvanic contact with the ground. The second pair of electrodes, known as potential electrodes, measure the potential established in the subsurface by the injected current. The midpoint of the array is kept fixed while the distance of the current electrodes is progressively increased. This causes current lines to penetrate greater depths, depending on the vertical distribution of the conductivity (Lowrie, 2007).

A total of 11 VES data were collected at the investigated sites (Figure 16 B). Table 4 lists the location and the maximum AB/2 for each VES. Resistivity surveys were conducted using the SYSCAL R2 (IRIS, France) resistivity imaging system (Figure 19). A Schlumberger electrode array was used with a maximum current electrode spacing of 316.2 m.

Table 4: VES's acquisition locations and current electrode separation.

| Wadi Name | VES | Longitude (degree) | Latitude (degree) | AB/2 (m) |
|---|---|---|---|---|
| **Ghreaba** | VES 1 | 33.97608 | 28.57564 | 316.2 |
| **Elsheikh** | VES 2 | 33.99486 | 28.571 | 316.2 |
| **Sudud** | VES 3 | 33.99997 | 28.56278 | 215.4 |
| | VES 4 | 34.00406 | 28.55892 | 215.4 |
| **Elsheikh** | VES 5 | 33.99142 | 28.58444 | 316.2 |
| | VES 6 | 33.99558 | 28.59708 | 215.4 |
| | VES 7 | 33.99153 | 28.65461 | 316.2 |
| | VES 8 | 33.99111 | 28.66575 | 316.2 |
| | VES 9 | 33.98517 | 28.68847 | 316.2 |
| **Elfuria** | VES 10 | 33.89325 | 28.65308 | 100 |
| **Elsheikh** | VES 11 | 33.99583 | 28.62906 | 316.2 |

Because of the field conditions, there was very high contact resistance during the survey. Saltwater was used around each electrode (Figure 19 C). Resistivity inversion models were conducted using the IX1D v3 Interpex software (Figure 20). These models were used to characterize the thickness of, and the depth to, the saturated zone in each location (Figure 28).

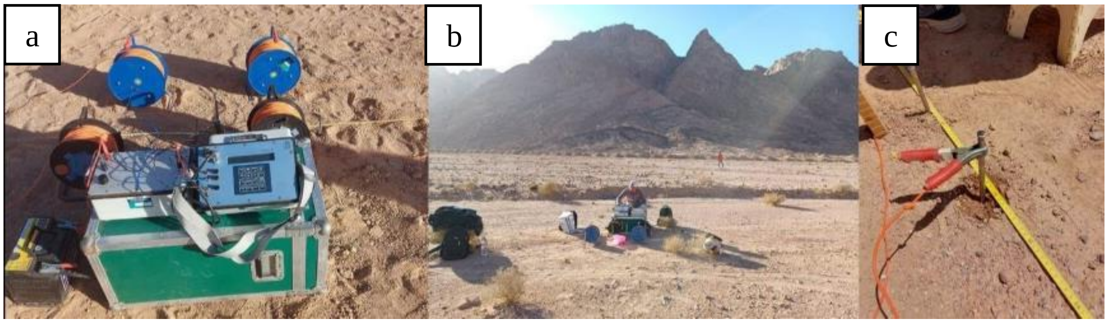


Figure 19: (a) Field image illustrates the components of the SYSCAL R2 resistivity imaging system; (b) Image displays the collection of resistivity data at one of the investigated sites; and (c) Image demonstrates the addition of saltwater to the current electrode to enhance coupling.

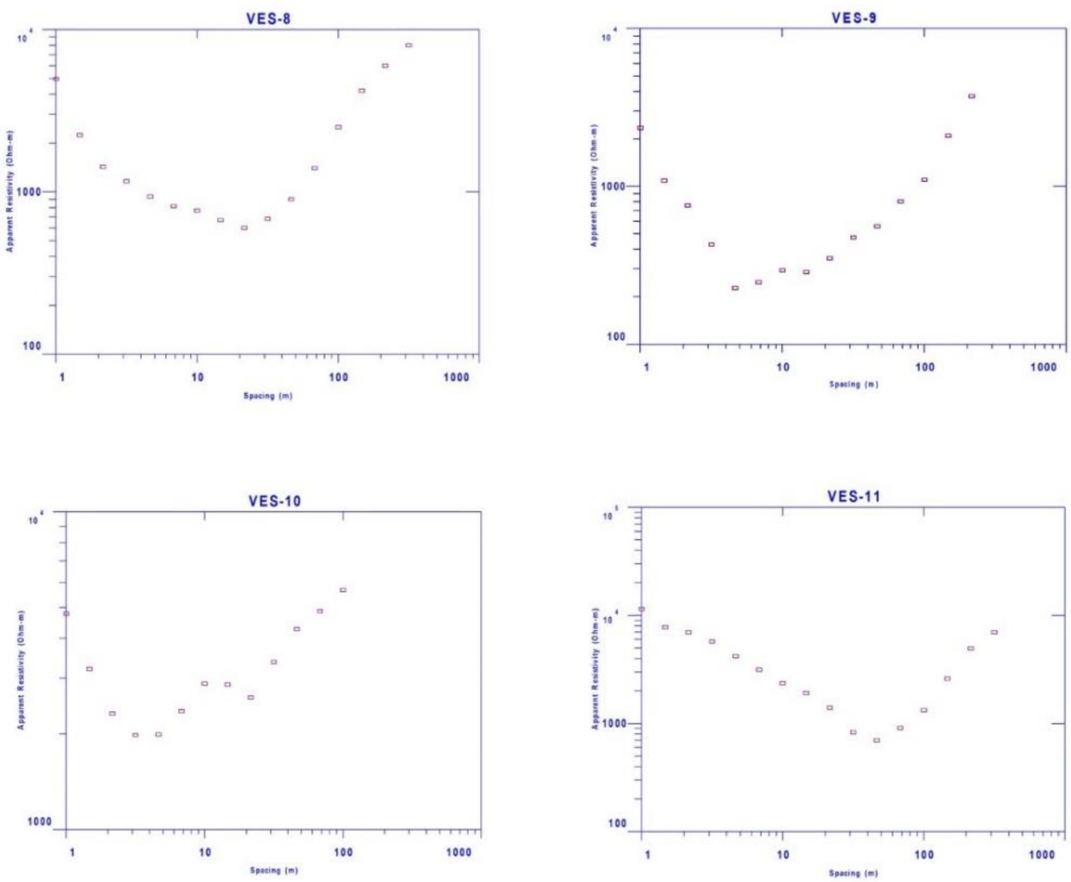


Figure 20: Examples of raw resistivity data collected at the study area.

### 3.3.3 Seismic Refraction (SR) Profiles

Because there is often a significant difference in seismic velocity between the overburden and the bedrock, the seismic refraction method has the potential to be used as an exploratory tool for groundwater in basement terrain areas (Olayinka, 1992). The seismic refraction technique measures the time it takes for a compressional wave produced by a sound source to travel through the subsurface layers before being refracted again to geophones (receivers) placed on the surface (Figure 22 C). Subsurface geology can be identified by measuring the sound wave's travel time and using the physics that govern sound propagation. As a result, measured distances and travel times will make up the field data. Velocity variations and depths to specific layers can be determined and modeled using this time-distance information (Haeni, 1988). Seismic refraction techniques have been successfully used in hydrogeological investigations across the globe (Abdelrahman et al., 2017; Azhar et al., 2019; Genedi & Youssef, 2023; Grelle & Guadagno, 2009; Murad et al., 2014; Khalil et al., 2008).

Seismic refraction surveying was conducted at locations showing in Figure 16 C. A total of 15 seismic profiles were collected (Table 5). Multichannel, digital seismic data were recorded using the Summit X One 48-channel seismograph system (Figure 22A and 22B). For each seismic profile, geometry parameters (geophone interval, shot location, units), acquisition parameters (sample interval, record length, delay), and filter parameters (acquisition filters, preamp gains, stacking) were adjusted. The hammer-type energy source was utilized with geophone and shot point spacings ranging from 2 to 5 m and 6 to 20 m, respectively (Table 6).

Table 5: SR profiles' locations and lengths.

| Wadi Name | Profile Name | Start point | | End point | | Length (m) |
|---|---|---|---|---|---|---|
| | | Longitude (degree) | Latitude (degree) | Longitude (degree) | Latitude (degree) | |
| Sudud | P1 | 34.0044 | 28.56008 | 34.00211 | 28.55941 | 235 |
| | P2 | 34.00038 | 28.56433 | 33.99972 | 28.56245 | 235 |
| Isbaeya | P3 | 33.99552 | 28.56527 | 33.99533 | 28.5675 | 235 |
| Ghreaba | P4 | 33.96603 | 28.56737 | 33.9677 | 28.56885 | 235 |
| | P5 | 33.97553 | 28.57486 | 33.97678 | 28.57533 | 94 |
| Elsheikh | P6 | 33.99142 | 28.60989 | 33.99181 | 28.612 | 235 |
| | P7 | 33.99543 | 28.59508 | 33.99541 | 28.59716 | 235 |
| | P8 | 33.99154 | 28.58452 | 33.99167 | 28.58238 | 235 |
| | P9 | 33.99164 | 28.61014 | 33.99258 | 28.61014 | 94 |
| | P10 | 33.99826 | 28.62901 | 33.99783 | 28.63116 | 235 |
| | P11 | 33.99161 | 28.65484 | 33.99183 | 28.65277 | 235 |
| | P12 | 33.99116 | 28.66639 | 33.99381 | 28.66414 | 235 |
| | P13 | 33.98675 | 28.68894 | 33.98431 | 28.68889 | 235 |
| Elfuria | P14 | 33.90811 | 28.65775 | 33.90961 | 28.65928 | 235 |
| | P15 | 33.89278 | 28.6515 | 33.89314 | 28.65356 | 235 |

The Summit X One system components (Figures 21 and 22A) are (1) SUMMIT X One Data Collector (DC): powers the digitizer units and regulates data transmission over the line cable. It also serves as an interface between neighboring line segments to the controlling PC and the repeater unit; (2) SUMMIT X One Remote Unit (RU): a digitizer unit located near the geophone. It can connect to any point along the line cable; (3) SUMMIT X One-Line Cable: a two-wire telemetry cable with a specialized self-healing coating for data transmission and power distribution; (4) SUMMIT X One Trigger Unit (TU): an optional accessory unit that feeds the trigger signal to the X One system close to the seismic source rather than long trigger extension cables connected to the nearest DC. The TU, like standard remote units, can connect to the line cable anywhere and thus move with the source (Figure 21).

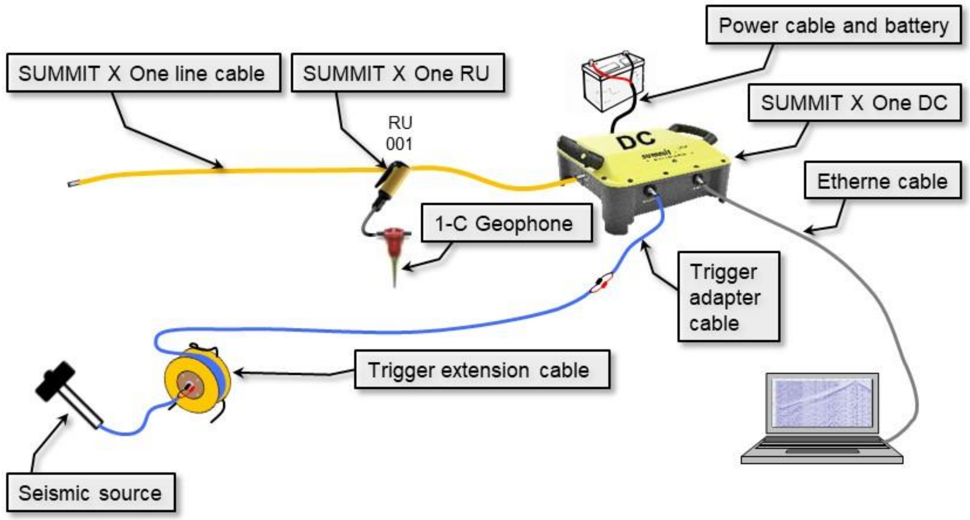


Figure 21: Summit X One system components.

Table 6: Seismic refraction data acquisition parameters.

| Parameter | Value |
|---|---|
| **Geophone interval (m)** | 2 - 5 |
| **Shot location (m)** | 6 – 20 |
| **Shots per profile** | 12 - 15 |
| **Sampling interval (ms)** | 1/16 |
| **Recording time (ms)** | 2000 |
| **Pre-Trigger (ms)** | 0 |
| **Stack count** | 3 - 5 |
| **Gain (dB)** | Low |
| **Polarity** | Seg |

Seismic refraction records were displayed, and the first arrivals were picked using the Geometrics SeisImager software (Pickwin Module) (Figure 23). The resulting travel-time curves (Figure 32) were interpreted and modeled using the same software (Plotrefa Module). The resulting models map the P-wave velocity structure of the subsurface. The velocity model was used to map the water table, the thickness of the saturated section, and the depth of basement rocks in the investigated sites (Figure 33).

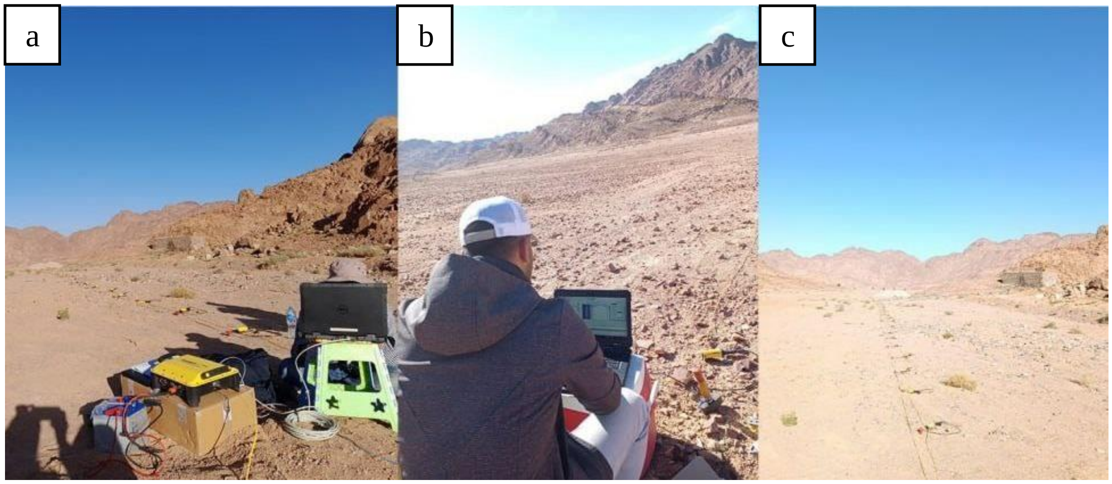


Figure 22: (a) The Summit X One 48-channel seismograph system in the field; (b) Acquisition console with an activated trigger; and (c) Field setup of the 48-channel layout.

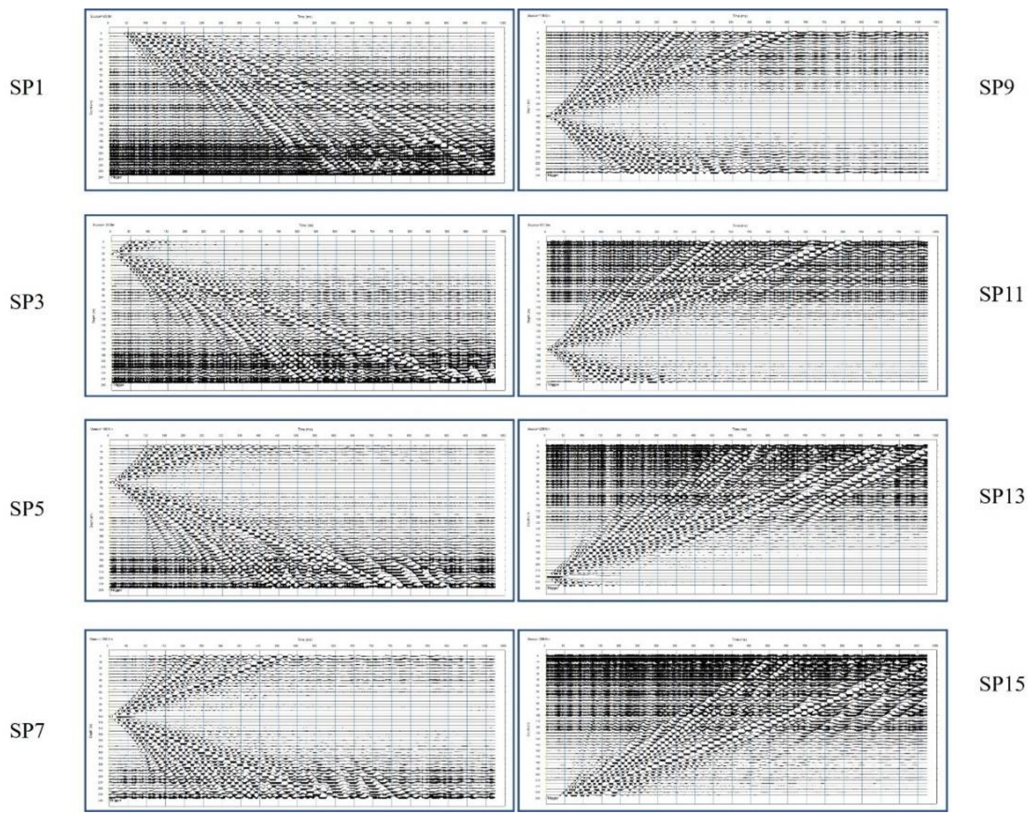


Figure 23: Examples of SR raw data from eight shot points (SP1, SP3, SP5, SP7, SP9, SP11, SP13, SP15) of seismic profile SR 1. The Y-axis represents distance in meters, and the X-axis represents time in milliseconds.

### 3.4 Groundwater Borehole Data

In this study, depth to water in nine groundwater wells were measured during the geophysical data collection process (Figure 25). Locations of these wells are shown on (Figure 24). The static groundwater levels, measured from the ground surface, in these wells ranged between 25.5 and 51 m (Table 7).

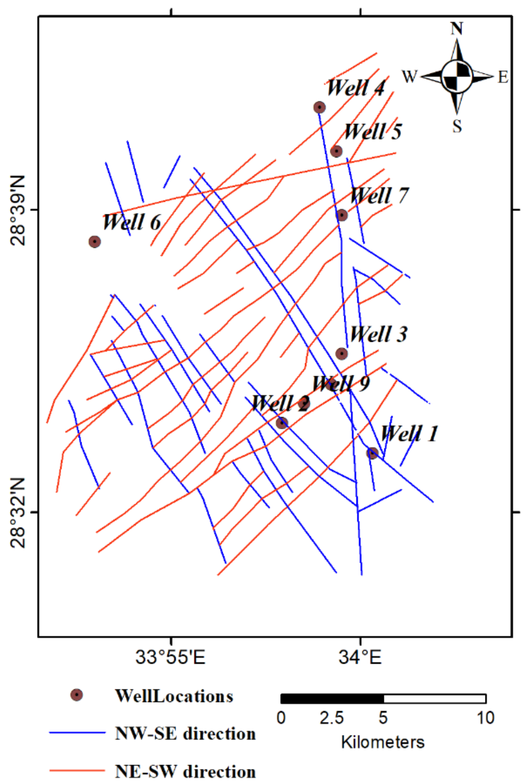


Figure 24: Location of drilled groundwater wells that we have recorded.

Table 7: Locations of groundwater wells and their depth to water table (DTW).

| Well | Local name | Longitude (degree) | Latitude (degree) | DTW (m) |
|---|---|---|---|---|
| **Well 1** | Sudud | 34.005364 | 28.556247 | 27.3 |
| **Well 2** | Haroun | 33.9656 | 28.567956 | 27.6 |
| **Well 3** | Zeituna | 33.99185 | 28.594622 | 44.6 |
| **Well 4** | Watia | 33.981961 | 28.689647 | 34.4 |
| **Well 5** | El-Halwagy | 33.989417 | 28.672806 | 27.4 |
| **Well 6** | Elsheikh Awad | 33.883258 | 28.637889 | 25.5 |
| **Well 7** | Unknown | 33.99183 | 28.64817 | 34 |
| **Well 8** | Unknown | 33.98722 | 28.58267 | 51 |
| **Well 9** | Unknown | 33.97522 | 28.57544 | 36 |

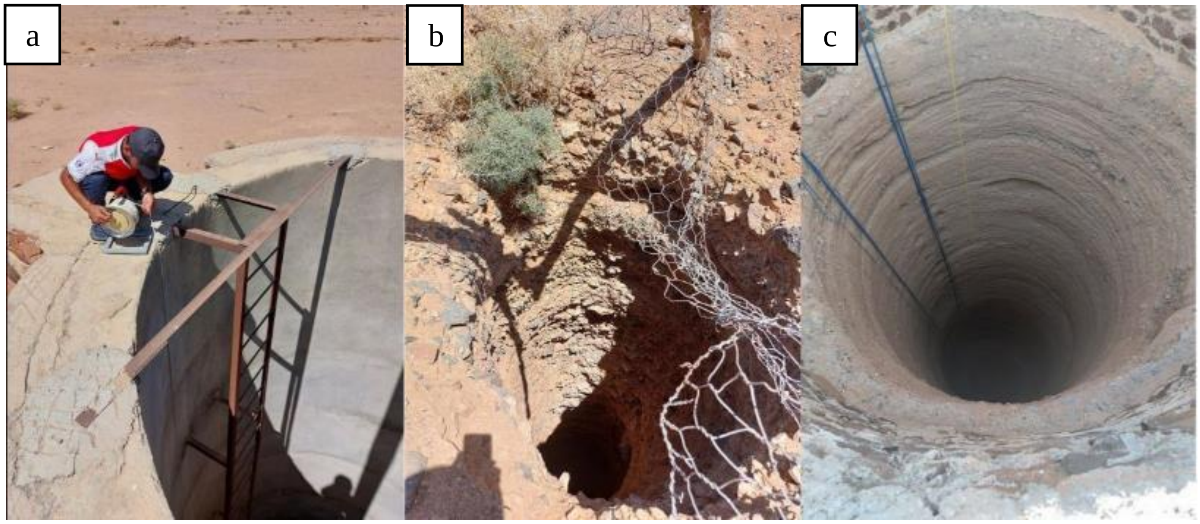


Figure 25: Examples of groundwater wells: (a) measuring the depth to the water table using the Sounder; (b) a dry well; (c) a productive well.

# 4. RESULTS

## 4.1 Optimal Recharge and Extraction Locations

The average annual rainfall over southern Sinai (Figure 9) ranges from 9.7 to 50.6 mm/yr. Higher rainfall rates (50 mm/yr) are concentrated over the central and northeastern parts of the study area (Figure 9), while western and southern parts experience relatively lower rainfall rates (12 mm/yr). High elevation areas experience higher rainfall compared to lower elevation regions due to several atmospheric and topographic factors. These include: (1) the orographic effect (orographic lifting), which contributes significantly to high rainfall in elevated areas. When moist air comes into contact with a mountain range or elevated terrain, it is forced to rise due to the barrier of the mountain. As the air rises, it cools, causing condensation and the formation of clouds. As a result, the clouds release moisture in the form of precipitation, resulting in heavier rainfall on the mountain's windward side; (2) higher condensation levels due to lower air pressure and cooler temperatures at higher elevations. Lower air pressure allows more moisture to enter, whereas cooler temperatures encourage condensation. All of these factors contribute to the formation of clouds and the subsequent release of moisture as rainfall (Chen et al., 2013; Houze, 2012). In terms of stream density, higher values (150 km/km$^2$) are concentrated over the northern and southern parts of the study area (Figure 13) while the western parts exhibit a relatively lower stream density (80 km/km$^2$). The central and northeastern parts of the study area are covered by gray and older granites as well as alluvial deposits (Figure 10B) which have been extensively affected by a dense fracture system. On the other hand, the southwestern parts of the study area are covered by pink and younger granites that are less affected by fractures. Faults and shear zones in southern Sinai are trending mainly in two directions: NW-SE and the NE-SW (Figure 11). Areas with higher fault density (85 km/km$^2$) are concentrated over north-central, southern, and northeastern parts of the study area (Figure 12). Conversely, regions with lower fault density are found in the western and the eastern parts of the study area (Figure 12). Regions with higher slopes (> 50°) are mainly found in the western and central parts of the study area (Figure 14), whereas the southeastern parts have lower slopes (< 10°).

Figure 26 shows potential recharge locations for the southern Sinai generated by the WOM. Based on the model outputs, potential recharge areas were classified as low (0.2–0.26), moderate (0.26–0.32), and high (>0.32). The low, moderate, and high potential recharge areas represent 47%, 37%, and 15% of the total study area, respectively. High potential recharge areas are spatially correlated with those that have porous lithology (alluvial deposits or older and fractured granites), high rainfall (50 mm/yr), high fault density (85 $km/km^2$), and high stream density (159 $km/km^2$) and have high number of fault intersections (>50). In contrast, low potential recharge areas are correlated with less porous lithology (e.g., younger granites), low rainfall (9.7 mm/yr), and low fault density (10 $km/km^2$) and have low number of fault intersections (<25).

Locations of productive wells, compiled from previously published studies, were utilized to confirm recharge locations. The locations of these wells are significantly correlated with the spatial distribution of areas that show high potential recharge (Figure 26).

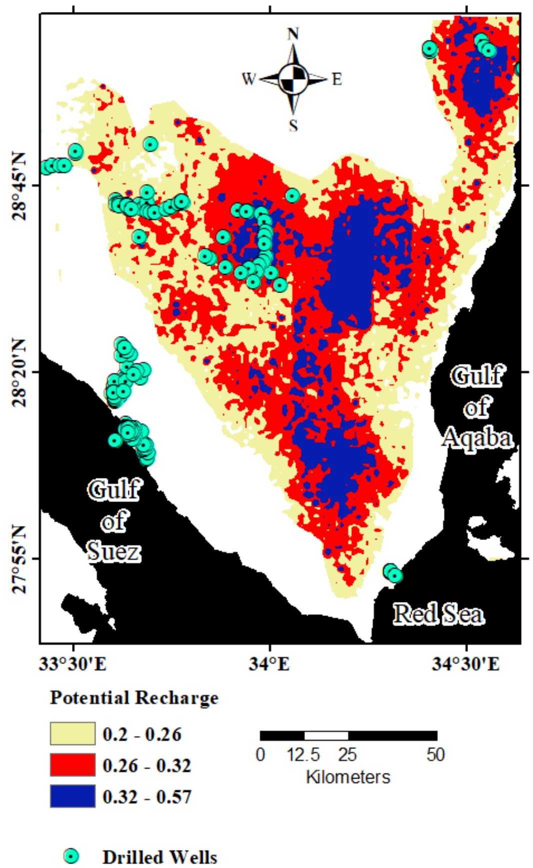


Figure 26: Spatial distribution of potential recharge locations, as well as the productive groundwater wells.

Figure 27 depicts the optimal locations for drilling productive groundwater wells. A total of 334 locations were mapped at the intersections of faults, shear zones, and faults/shear zones. Most of these wells (83%, or 274 wells) are located within high and moderate potential recharge areas (Figure 26). Intersections of geologic structures result in the development of intricate fracture networks in the subsurface. These fractures can act as conduits for the movement and storage of groundwater, providing pathways for water to accumulate and flow more freely (Mohamed et al., 2015). Fault/shear zones intersections can also create zones of increased porosity and permeability due to the intense tectonic activity and associated deformation. These zones can enhance groundwater storage and improve the ability of wells to extract water from the aquifer (Caine et al., 1996; Evans et al., 1997; Gudmundsson, 2000; Mohamed, 2015). In addition, fault intersections can create mixing zones where different water sources converge. These areas can have unique hydrogeochemical characteristics and may contain water that has undergone various interactions and mixing processes (EL-Rayes et al., 2015). Locations of productive wells, measured during the field data acquisition, were utilized to confirm extraction locations. The locations of these wells are significantly correlated with the spatial distribution of extraction locations (Figure 27).

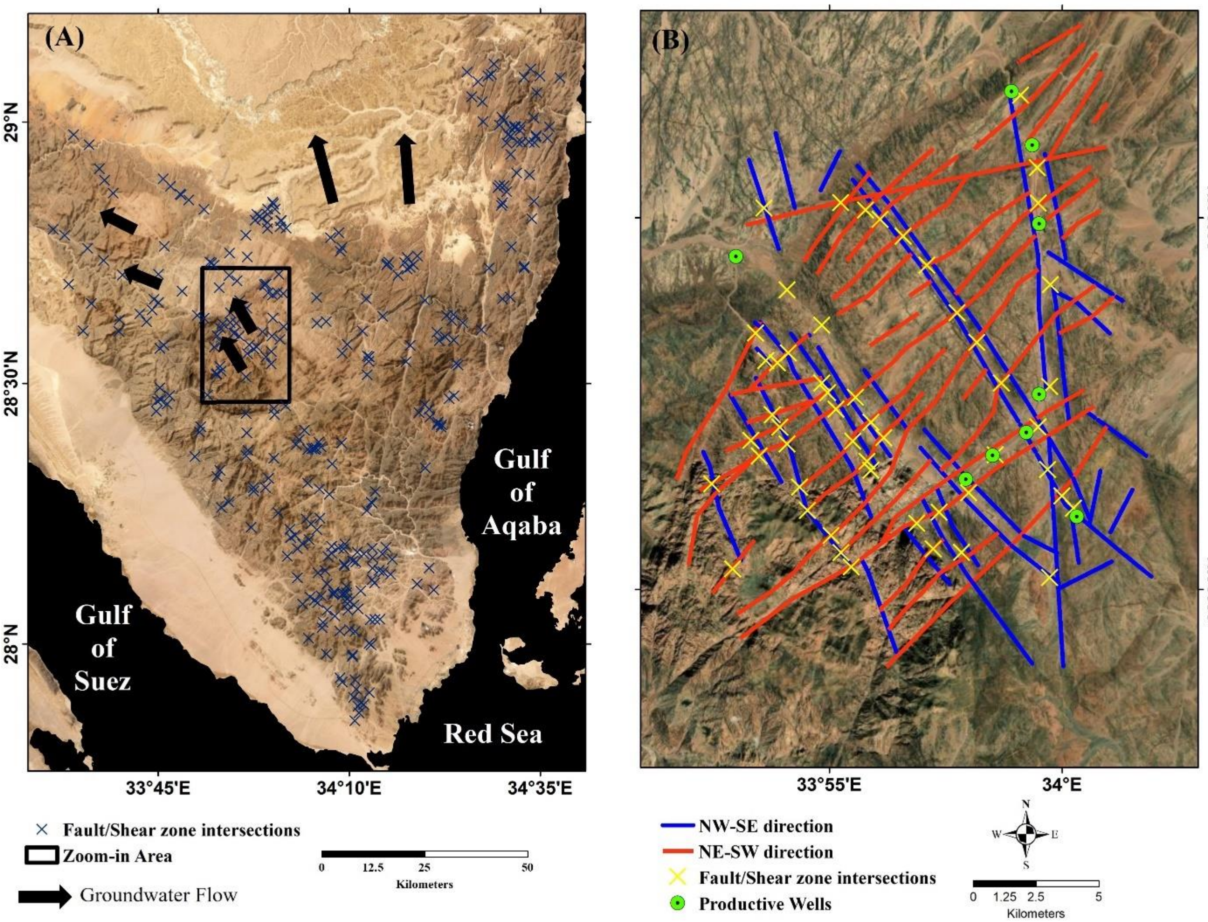


Figure 27: (A) Fault/Shear zone intersections as optimal locations for drilling groundwater wells and the regional groundwater flow direction (Abouelmagd et al., 2014; Mohamed et al., 2015); (B) Intersections over a zoomed area for a better visualization.

## 4.2 Structural Controls on Groundwater Accumulation and Flow in Basement Terrains

This section describes results of our geophysical surveys (VES, SR, and GPR) that were used to confirm the results from the remote sensing exercise mainly to identify subsurface geological features and characterize their influence on groundwater accumulation and flow.

### 4.2.1 Vertical Electrical Sounding (VES)

The interpretation of the 11 VESs collected in the study area reveals three main geoelectric layers (Figure 28). These geoelectric layers were defined as unsaturated sediments, saturated sediments, and basement rocks. The estimated root mean square (RMS) errors of the resulting models for the 11 VESs ranged from 4.6 to 20%, indicating a medium fit for the generated models (Figure 28).

Interpretation of the VESs data indicates that the resistivity of the unsaturated layer ranges between 830 and 8700 Ω.m, while the thickness varies between 1.5 and 10.5 m. This layer is composed of dry boulders, gravels, sands, and clays. The resistivity and thickness of the saturated sediment layer range between 220-420 Ω.m and 2-22 m, respectively. This is the aquifer unit in both alluvial and fractured basement systems. The basement rocks have resistivity values that range between 1840 and 26500 Ω.m, while their depth ranges between 8 and 31.5 m (Figure 28).

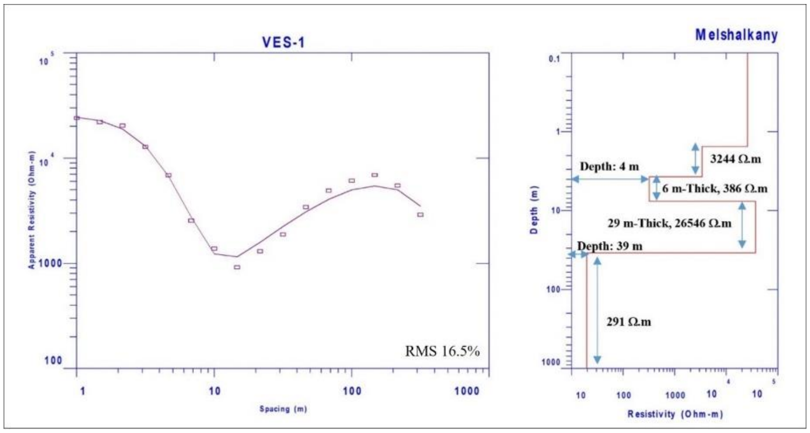
VES-1
Melshalkany
Apparent Resistivity (Ohm-m)
Spacing (m)
RMS 16.5%
Depth (m)
Resistivity (Ohm-m)
3244 Ω.m
Depth: 4 m
6 m-Thick, 386 Ω.m
29 m-Thick, 26546 Ω.m
Depth: 39 m
291 Ω.m

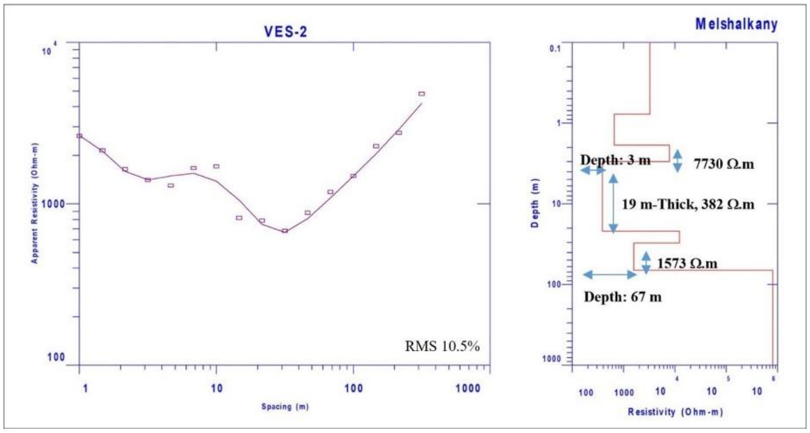
VES-2
Melshalkany
Apparent Resistivity (Ohm-m)
Spacing (m)
RMS 10.5%
Depth (m)
Resistivity (Ohm-m)
Depth: 3 m
7730 Ω.m
19 m-Thick, 382 Ω.m
1573 Ω.m
Depth: 67 m

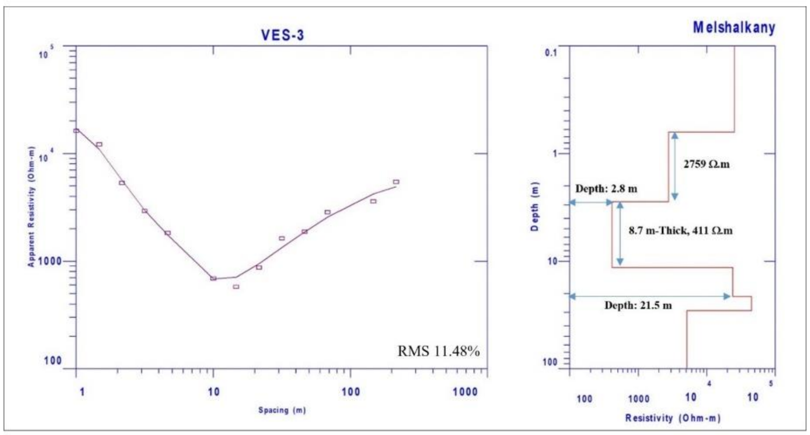
VES-3
Melshalkany
Apparent Resistivity (Ohm-m)
Spacing (m)
RMS 11.48%
Depth (m)
Resistivity (Ohm-m)
2759 Ω.m
Depth: 2.8 m
8.7 m-Thick, 411 Ω.m
Depth: 21.5 m

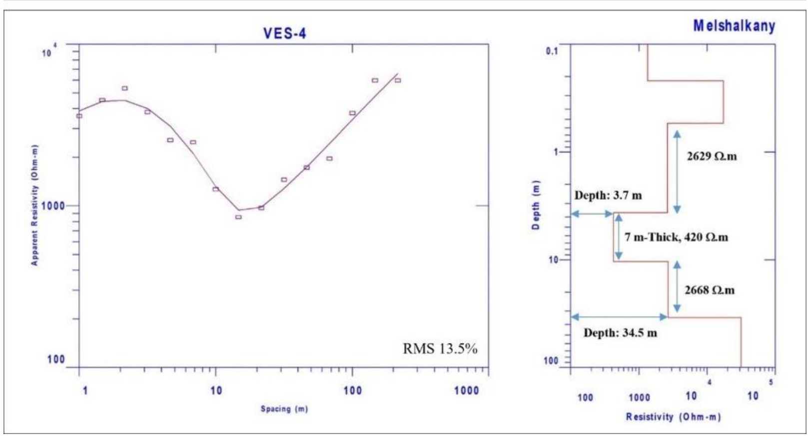
VES-4
Melshalkany
Apparent Resistivity (Ohm-m)
Spacing (m)
RMS 13.5%
Depth (m)
Resistivity (Ohm-m)
2629 Ω.m
Depth: 3.7 m
7 m-Thick, 420 Ω.m
2668 Ω.m
Depth: 34.5 m

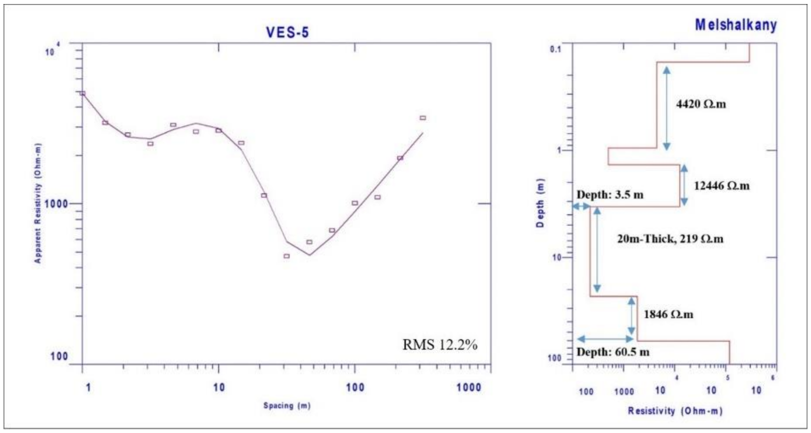
VES-5
Melshalkany
4420 Ω.m
12446 Ω.m
Depth: 3.5 m
20m-Thick, 219 Ω.m
1846 Ω.m
Depth: 60.5 m
RMS 12.2%
Apparent Resistivity (Ohm-m)
Spacing (m)
Depth (m)
Resistivity (Ohm-m)

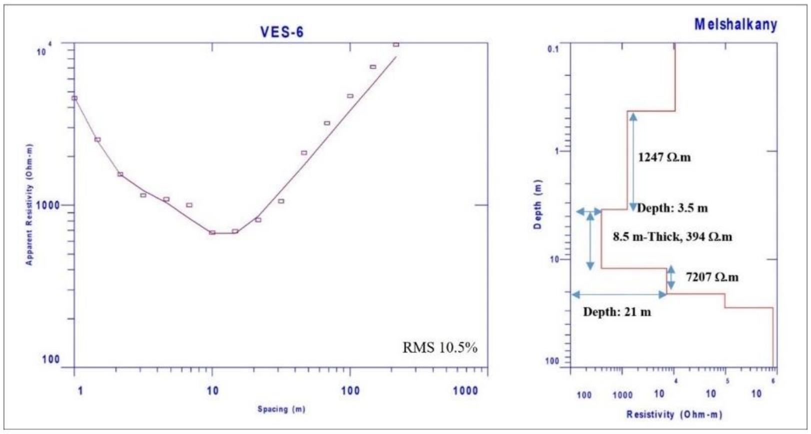
VES-6
Melshalkany
1247 Ω.m
Depth: 3.5 m
8.5 m-Thick, 394 Ω.m
7207 Ω.m
Depth: 21 m
RMS 10.5%
Apparent Resistivity (Ohm-m)
Spacing (m)
Depth (m)
Resistivity (Ohm-m)

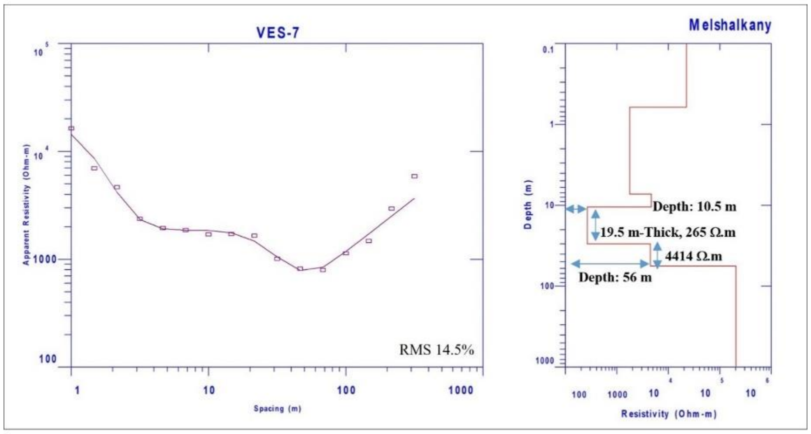
VES-7
Melshalkany
Depth: 10.5 m
19.5 m-Thick, 265 Ω.m
4414 Ω.m
Depth: 56 m
RMS 14.5%
Apparent Resistivity (Ohm-m)
Spacing (m)
Depth (m)
Resistivity (Ohm-m)

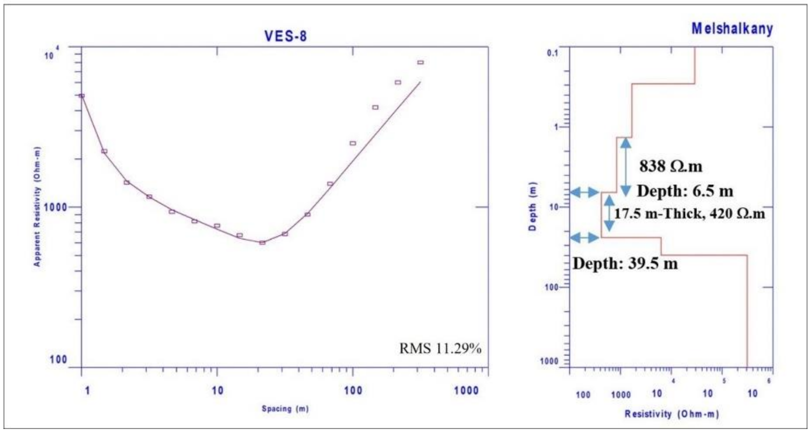
VES-8
Melshalkany
838 Ω.m
Depth: 6.5 m
17.5 m-Thick, 420 Ω.m
Depth: 39.5 m
RMS 11.29%
Apparent Resistivity (Ohm-m)
Spacing (m)
Depth (m)
Resistivity (Ohm-m)

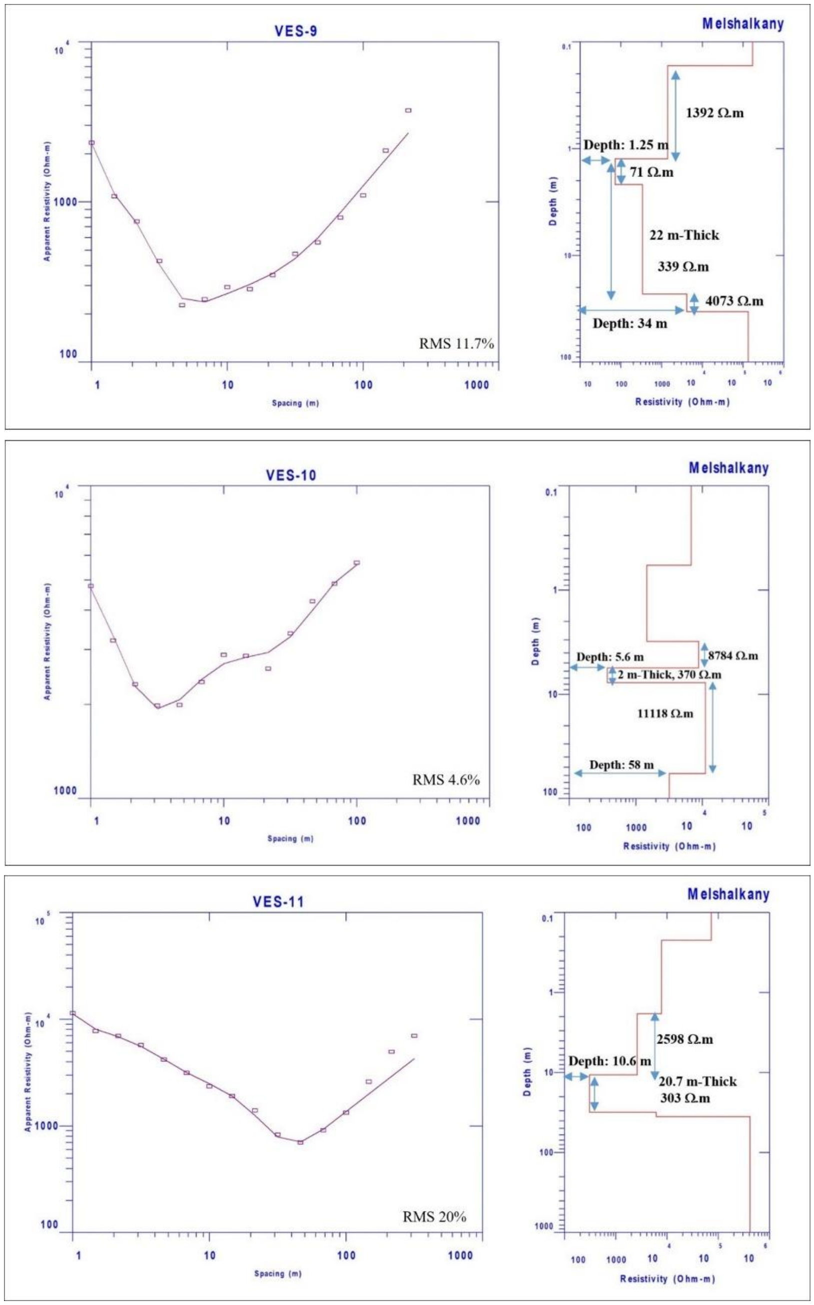


Figure 28: Modeled layer depth, thickness, and apparent resistivity, and the RMS values for 11 VESs collected in southern Sinai.

The groundwater levels, measured from the ground surface, extracted from the resistivity data demonstrated a strong correspondence with those extracted from nearby wells. The VES data collected in the vicinity of the well locations (e.g., VES 7 depth:10.5 m, VES 1 depth: 39 m) aligned well with the depth of the respective wells (Well 7: 34 m; Well 9: 36 m) (Figure 24). The other wells are located far away (500 to 1000 m) from the remaining VESs due to the nature of the field. The productive wells in the area are strategically positioned along fault and fault intersection zones. For instance, Wells 2 (DWT: 27.6 m) and Well 8 (DWT: 51 m, were actively pumping water right before the measurement time), are located at the intersection of two shear zones. Wells 1 (DWT: 27.3 m) and Well 4 (DWT: 34.4 m) are situated at the intersection of two faults, while Well 7 (DWT: 34 m) is positioned at the junction of a fault and a shear zone (Figure 24).

The resistivity, thickness, and depth to the saturated zone exhibit spatial variability. These variabilities are controlled mainly by the locations of geologic structures (e.g., faults and shear zones) and their intersections (Figure 29). Figures 30, and 31 show that where two or more faults, shear zones, and fault/shear zone intersection where present (e.g., VES 2, VES 3, VES 5, VES 7, VES 8, VES 9, VES 11), the saturated zone exhibited increased thickness (thickness: 18 ± 4 m) and shallower depth (depth 5.5 ± 3.5 m). The thickness of the saturated zone is reduced in areas with a low number of faults, shear zones, and fault/shear zone intersections (e.g., VES 4). Areas located away from faults, shear zones, and fault/shear zone intersections (e.g., VES 1, VES6, and VES10) exhibit a relatively thin saturated zone (thickness: 5.5 ± 2.5 m) at greater depth (depth 13 ± 15 m).

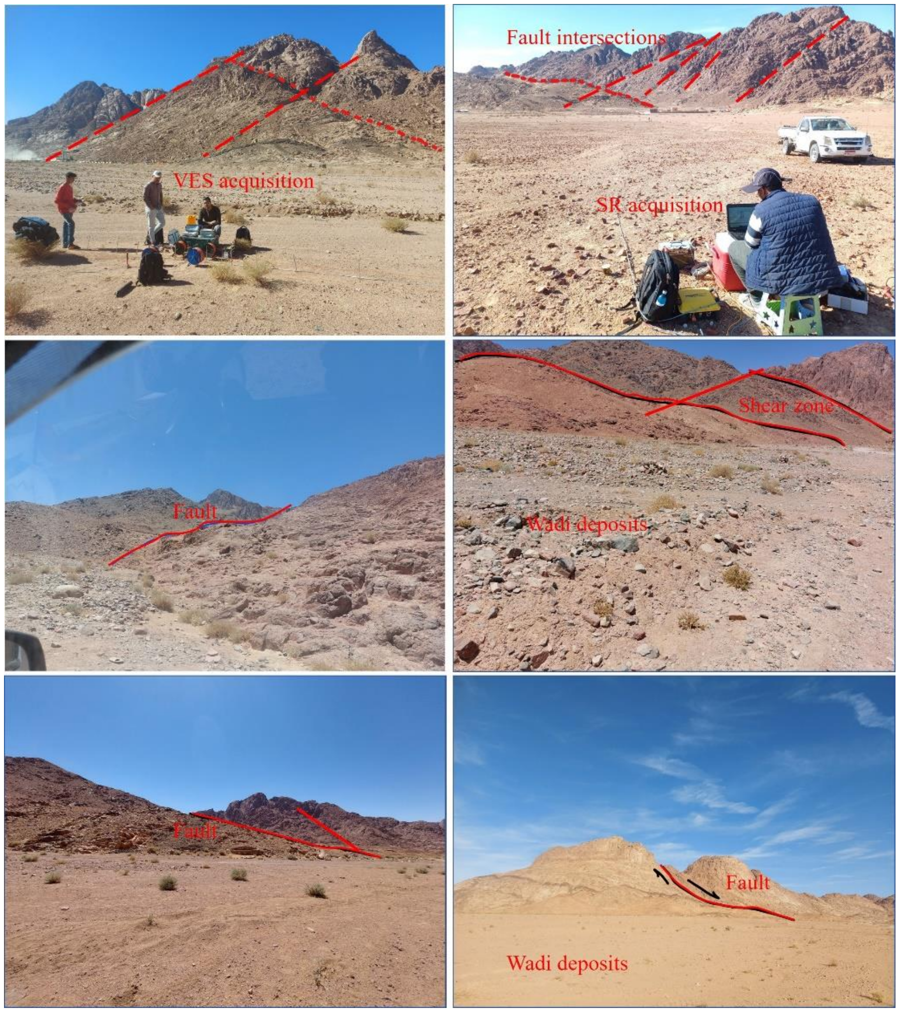


Figure 29: Field pictures showing faults/shear zones and their intersections.

The interpretation of the VES data provided compelling evidence supporting the notion that faults, shear zones, and fault/shear zone intersections serve as highly favorable locations for drilling sustainable groundwater wells. Thorough analysis of the VES data confirmed this assertion. Specifically, it revealed that these geological features are associated with certain characteristics that make them optimal for groundwater extraction. One significant finding was the observation of a thick and shallow saturated zone at these fault, shear zone, and fault/shear zone intersection sites. The VES data analysis consistently demonstrated that the saturated zone in these areas exhibited greater thickness compared to other locations. This attribute is highly advantageous as it indicates a substantial volume of groundwater that can be accessed and utilized. Furthermore, the shallow nature of the saturated zone at these intersections further strengthens their suitability for well drilling. The shallowness implies that the depth required to reach the groundwater is relatively less, which in turn reduces drilling costs and facilitates the extraction process. This favorable characteristic also enhances the overall efficiency and accessibility of the groundwater resource. The convergence of faults, shear zones, and fault/shear zone intersections in these areas creates a unique synergy that fosters ideal conditions for groundwater accumulation. The geological complexities resulting from these intersections play a crucial role in the hydrogeological system, allowing for the efficient capture and storage of water resources. This interaction facilitates the replenishment of the saturated zone, ensuring a sustainable supply of groundwater. The groundwater flow within saturated zones is primarily influenced by surface gradients (e.g., slope). The surface gradient influences the hydraulic head, which is the potential energy of the groundwater system. Groundwater tends to flow from areas of higher hydraulic head to those with lower hydraulic head. This flow occurs along the direction of the ground surface gradient, as it represents the natural downward slope guiding the movement of water.

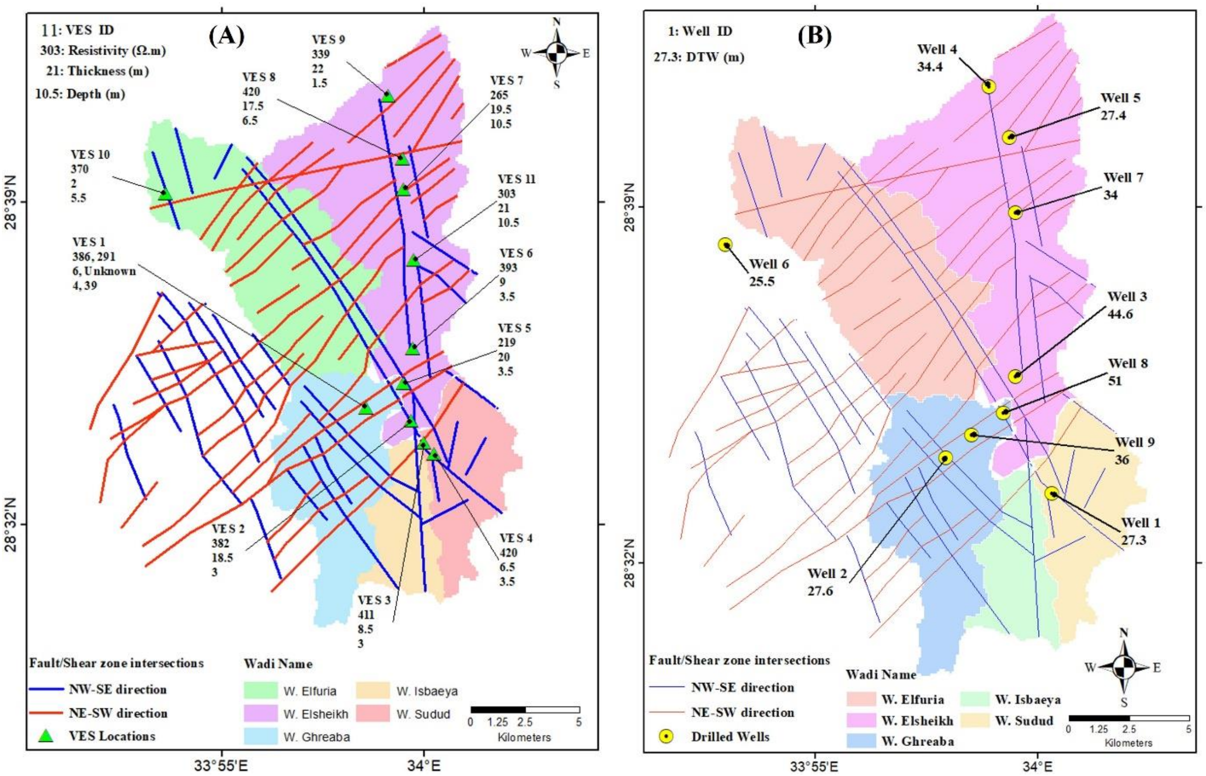


Figure 30: (A) Spatial variation in the resistivity, thickness, and depth to the saturated zone as indicated from interpretation of VESs data; (B) Location of drilled groundwater wells and their depth to water table (DTW).

The interpreted VES stations were used to create a geoelectric cross-section from south to north along Wadi Sudud and Wadi Elsheikh (Figure 31). The southern portion of the cross-section has a higher elevation (up to 1566 m) than the northern portion, which has a lower elevation (1273 m). The elevation difference has a significant role in the direction of groundwater flow.

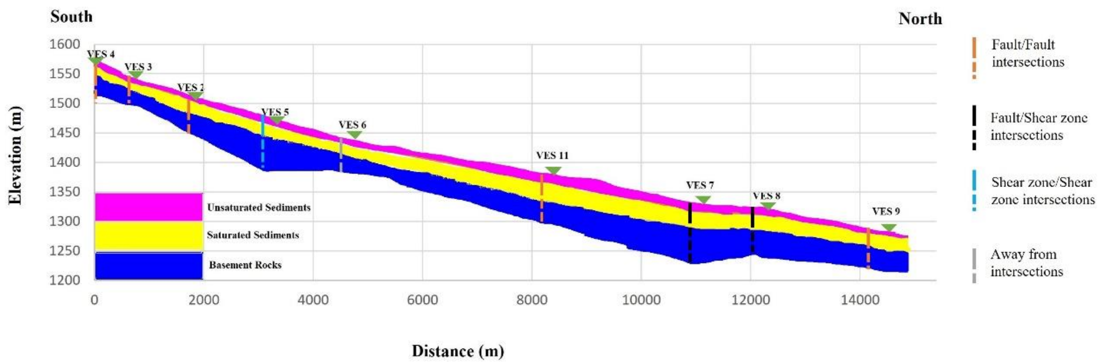


Figure 31: South-to-north geoelectric cross-section combining VES 4, VES3, VES 2, VES 5, VES 6, VES 11, VES 7, 8, and VES 9. The southern portion has higher elevation up to 1566 m, while the northern portion has the lower elevation of 1273 m.

### 4.2.2 Seismic Refraction (SR) Profiles

Before interpreting the seismic refraction data, we performed an extensive compilation of primary wave velocity (Vp) values for saturation zones from seismic refraction studies conducted in comparable geological and climatic settings. Our results indicate that the Vp values for saturation zones fall within the range of 1325-1680 m/s (as shown in Table 8), which is consistent with previous findings reported by Shendi and El-Rayes (1992). A summary of the literature research is provided in Table 8.

Table 8: Seismic refraction studies with interpreted Vp values for saturation zones. Modified after (Azhar et al., 2019).

| No. | Authors | Vp (m/s) | Remarks |
|---|---|---|---|
| 1 | (Shendi & El-Rayes, 1992) | 1400-2500 | Basement aquifer |
| 2 | (Abdelrahman et al., 2017) | 900-1800 | Basement aquifer |
| 3 | (Adelinet et al., 2018) | 2400-2500 | Weathered basaltic aquifer |
| 4 | (Adeoti et al., 2012) | 2200-2300 | Sandy aquifer |
| 5 | (Araffa et al., 2017) | 1500-1900 | Sandstone/shale aquifers |
| 6 | (Becht et al., 2007) | 1750-2000 | Gravel aquifer |
| 8 | (Desper et al., 2015) | 1500-2000 | Quaternary sediments |
| 9 | (Grelle & Guadagno, 2009) | 1500 | Gravely sand aquifer |
| 10 | (Kim & Kim, 2008) | 1300-1400 | Sandy gravel aquifer |
| 11 | (Murad et al., 2014) | 1430-1600 | Alluvial gravel sand aquifer |
| 12 | (Pasquet et al., 2015) | 1500-1600 | Saturated sediments |

The travel time-distance plots for 12 out of 15 SR profiles are shown in Figure 32. The remaining 3 SR profiles were extremely noisy and challenging to process. These plots clearly depict three distinct slope breaks, indicating the presence of three subsurface layers characterized by distinctive velocities. The top layer is represented by the pink color, the second layer by the green color, and the bottom layer by the blue color. The RMSE error for all plots ranged between 8% and 21%.

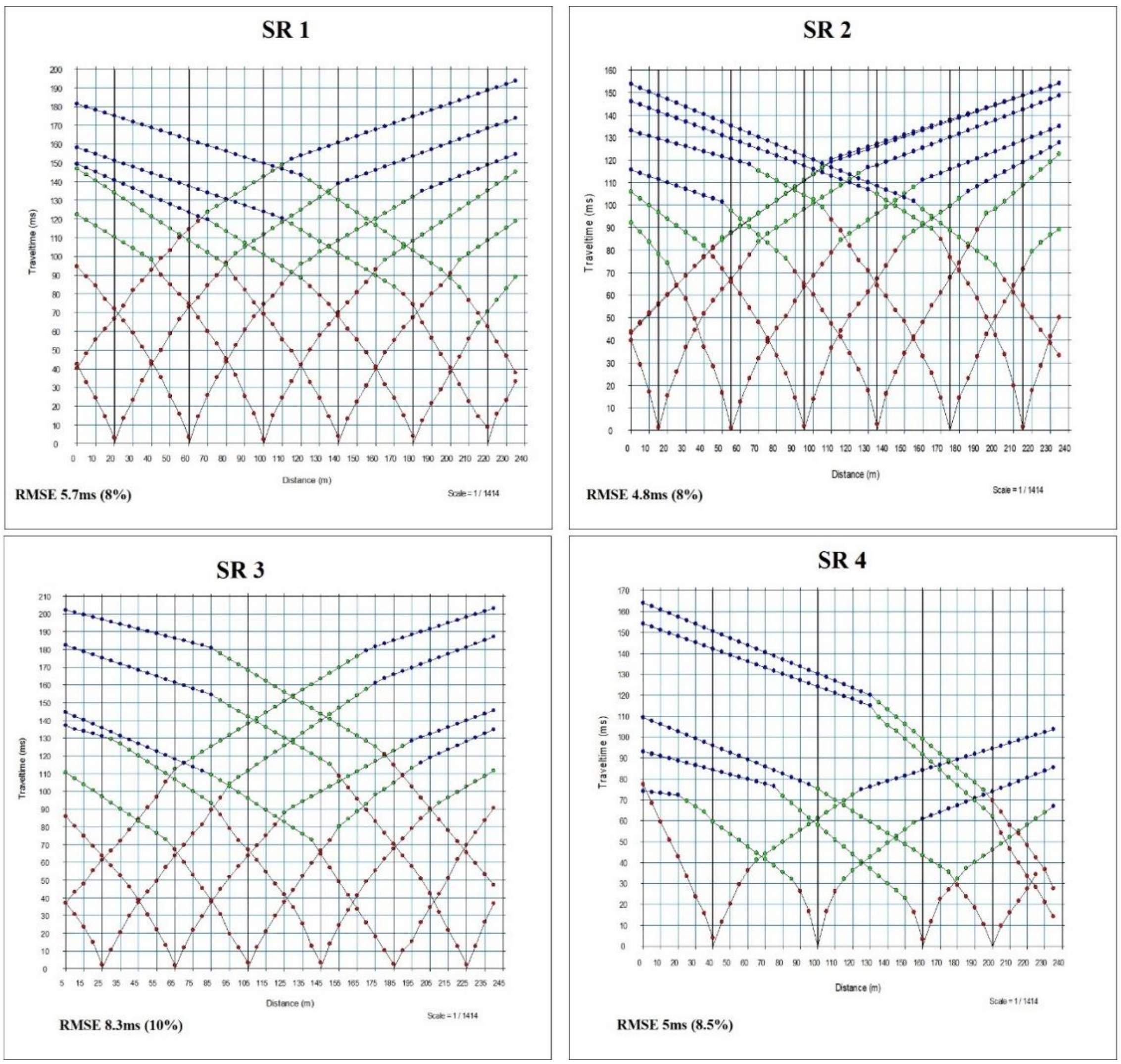

**SR 5**

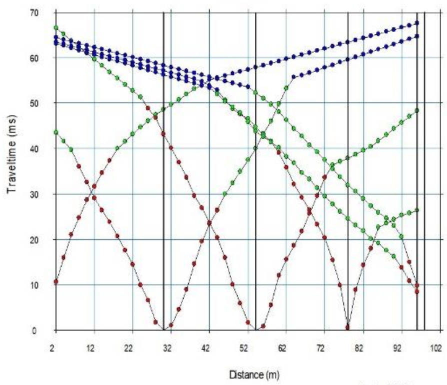


**RMSE 4.89ms (19%)**

**SR 6**

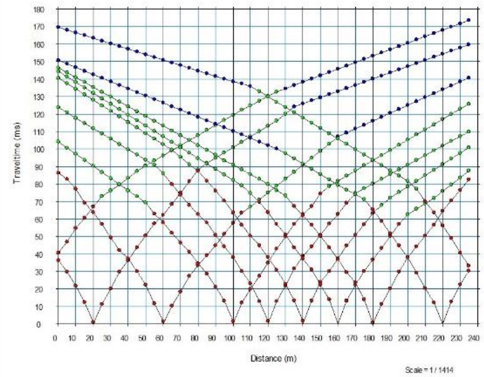


**RMSE 6ms (8%)**

**SR 8**

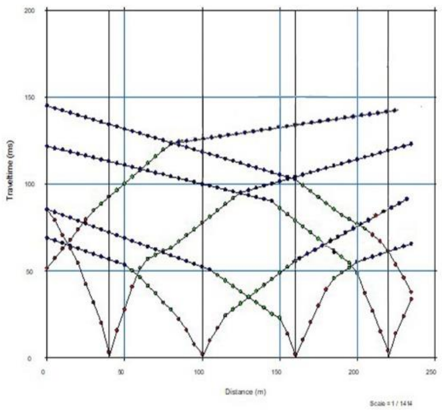


**RMSE 13ms (20%)**

**SR 10**

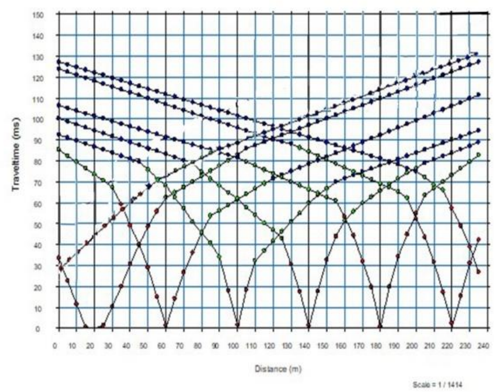


**RMSE 5ms (17%)**

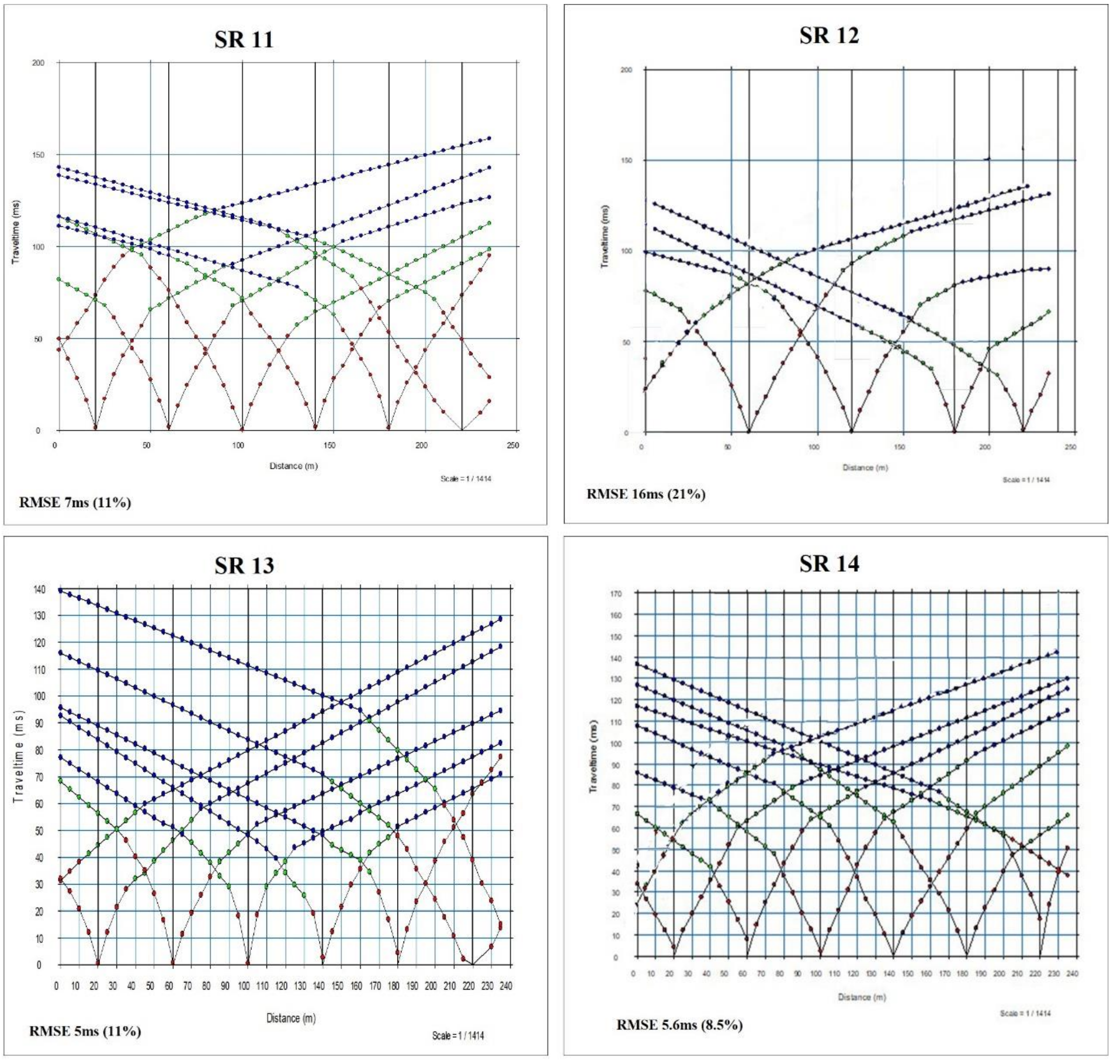


Figure 32: Travel time-distance plots showing three main layers. The Y-axis represents travel time in milliseconds, and the X-axis represents distance in meters. The top layer is represented by the pink color, the second layer by the green color, and the bottom layer by the blue color.

Interpretation of SR surveys reveals the presence of three distinct main layers (Figure 33). The weathered unsaturated layer above the saturated zone exhibited a seismic velocity range of 405-547 m/s, indicating its lower velocity characteristics. In contrast, the saturated zone demonstrated a higher velocity range of 1325-1680 m/s, while the underlying basement rocks displayed an even greater velocity range of 1818-4810 m/s. The saturated zones exhibited average depths ranging from 5 to 15.5 m, while their thicknesses ranged from 14.5 to 24.5 m.

Depths to saturated zones, as derived from the seismic refraction data (Figures 33 and 34), exhibit a good correlation with measurements obtained from nearby wells. For instance, profile SR 4 displays average depth to the saturated zone of 5 m, average thickness of 24.5 m, which closely aligns with the measurement taken at Well 2 (DTW: 27.6 m). However, this correlation applies only to wells situated in close proximity to the seismic profiles.

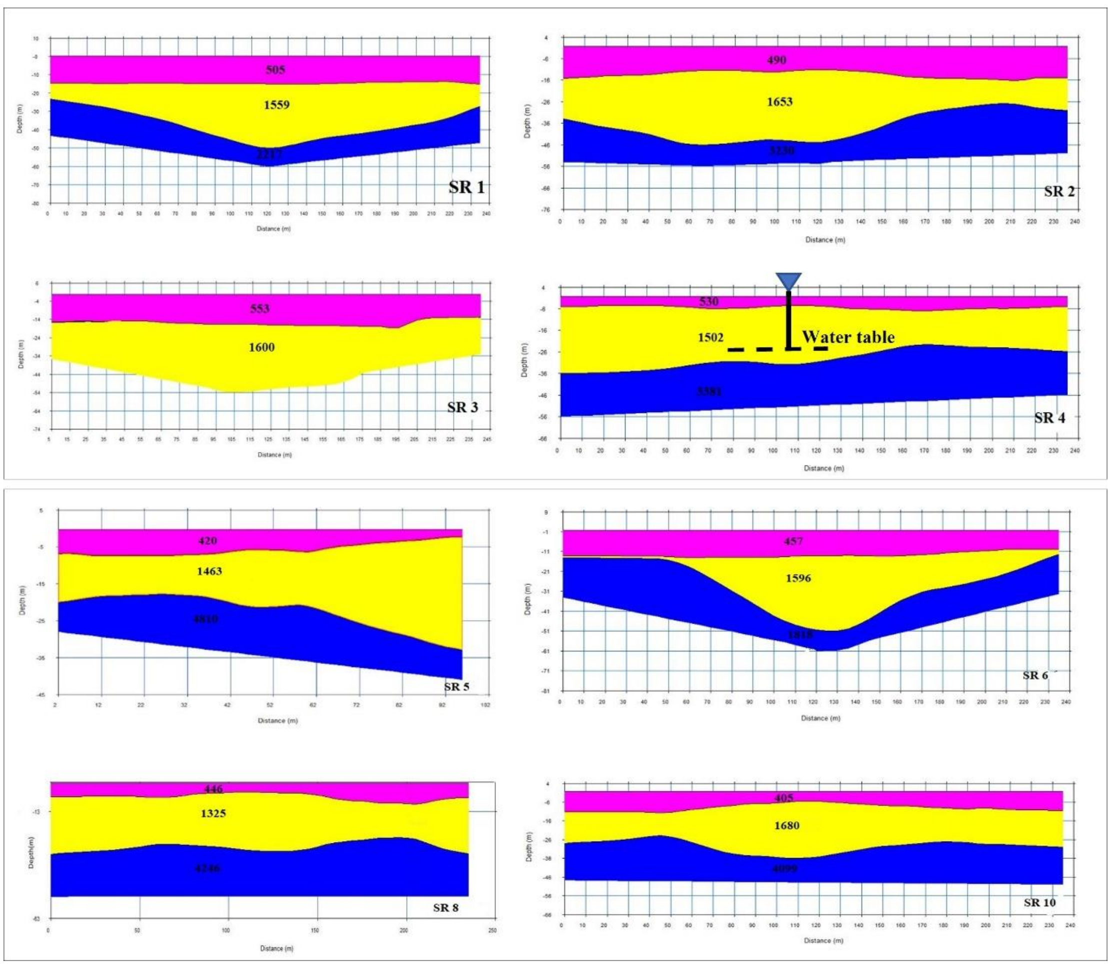

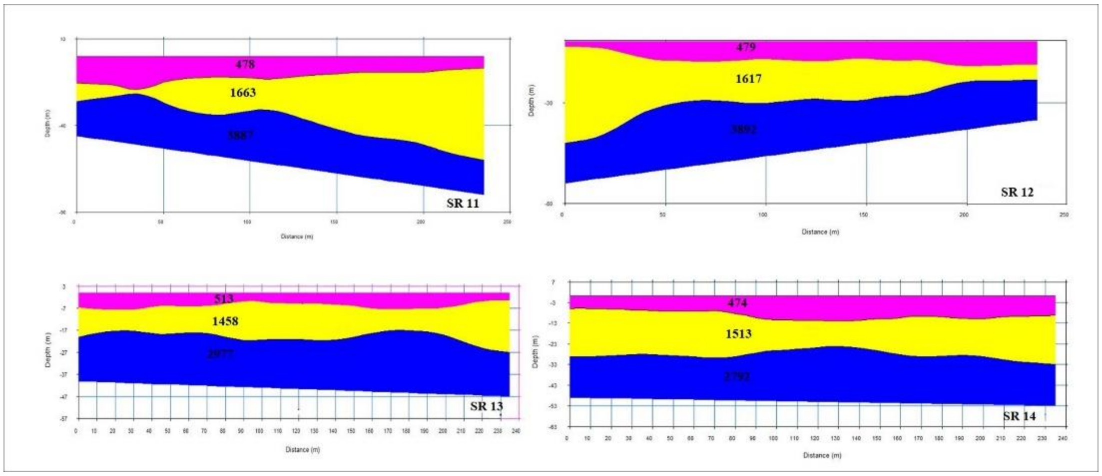


Figure 33: Seismic cross sections show three subsurface layers: unsaturated sediments (purple), saturated sediments (yellow), and basement rocks (blue). SR 4 shows the depth to the water table from the nearest well (Well 2).

The interpretation of the SR data indicated an increase in the thickness of alluvial sediments (including both unsaturated and saturated layers) as one moves away from the basement rocks and towards the center of each wadi. For instance, profiles SR 5, SR 11, and SR 12 demonstrate an average alluvial thickness of 45 ± 12 m at the wadi's center, in contrast to 21 ± 3 m the wadi's boundaries. It is expected that the basement rocks would be deeper at the center of the wadi. Profile SR 6, for example, exhibits a pattern where the basement rocks are shallower (12 m) at the profile's boundary and deeper (45 m) at the center of the profile.

Similar to the results obtained from VESs, the saturated zone derived from the SR surveys also exhibits spatial variability, primarily influenced by the locations and intersections of fault/shear zones (Figure 34). For example, profiles SR 2, SR 11, and SR 12 are located at the intersection of fault and shear zone. At these locations, the average thickness of the saturated zone is 23 ± 0.2 m, with an average depth of 11 ± 2 m. Profiles SR 1, SR 3, SR 6, and SR 10 are located at the intersection of two faults. At these locations, the average thickness of the saturated zone is

20 ± 3 m, with an average depth of 12.5 ± 2.5 m. Profiles SR4, and SR 8 are located at the intersection of two shear zones. At these locations, the average thickness of the saturated zone is 23.5 ± 1 m, with an average depth of 5.75 ± 0.75 m. Profiles SR 5, SR13, and SR 14 are close to the intersection of faults/shear zones. At these locations, the average thickness of the saturated zone is 16 ± 2 m, with an average depth of 7 ± 2 m. Additional compelling evidence, provided by the interpretation of SR data, supporting the notion that faults, shear zones, and fault/shear zone intersections serve as highly favorable locations for drilling sustainable groundwater wells.

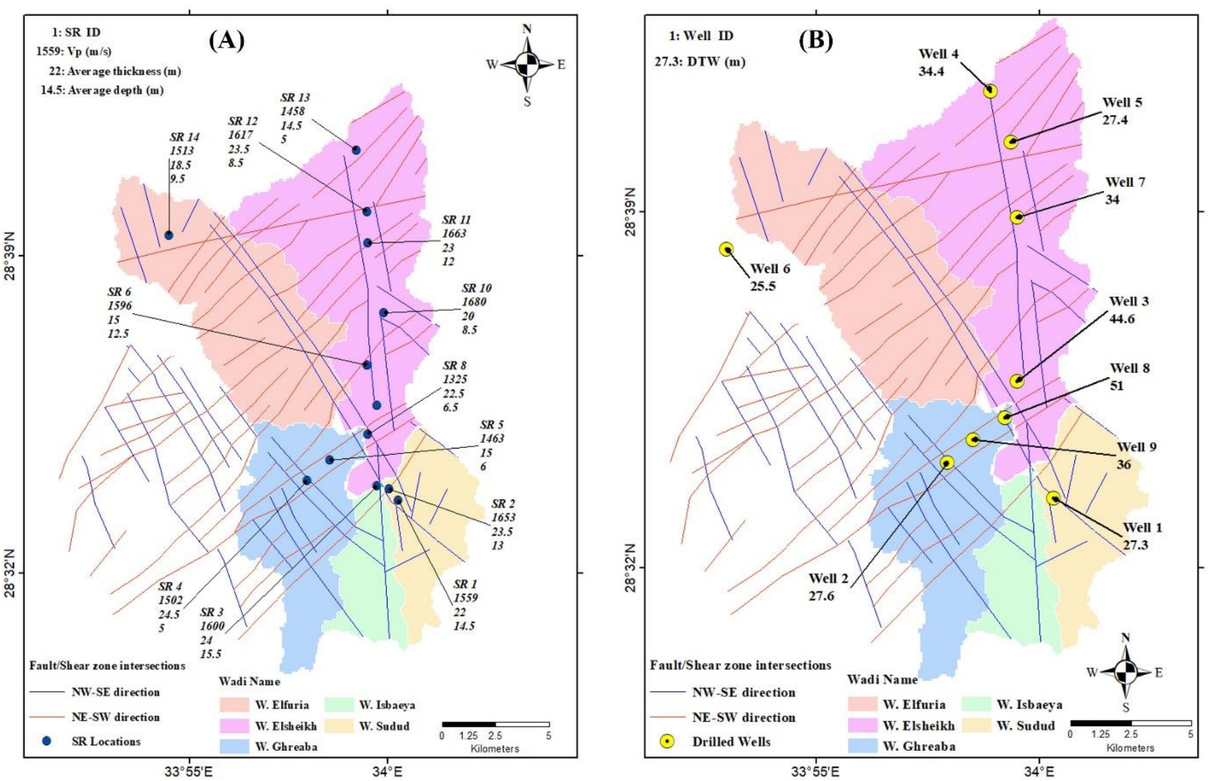


Figure 34: (A) Spatial variation in the velocity, thickness, and depth to the saturated zone as indicated from interpretation of SR data; (B) Location of drilled groundwater wells and their depth to water table (DTW).

### 4.2.3 Ground Penetrating Radar (GPR)

Unfortunately, the GPR data did not show anything coherent below the first 100-150 samples (depth: 10-15 m at a dielectric constant of 2) (Figure 35). The raw GPR data below sample 100 are dominated by antenna ringing at about 29 MHz, which is what appears when there is no other signal to overpower the ringing. Ringing refers to the appearance of oscillations or wavy patterns in the GPR signal, typically appearing as high-frequency reflections. Ringing is usually caused by an impedance mismatch between the near-surface materials and the antenna impedance. This can happen when the earth is highly resistive, or else highly conductive (pipes or power poles). The 100 MHz antennas are manufactured with a fixed impedance by using four resistors at the corners of the bowtie that connect to the shield above. These are on the order of 100 Ohms for the 100 MHz antennae. So, if the ground surface is much lower resistivity or much higher resistivity, there will be a ringing signal. We have both cases in the Southern Sinai wadies, a general background ringing probably due to high resistivity subsurface materials, and local ringing when passing by power poles.

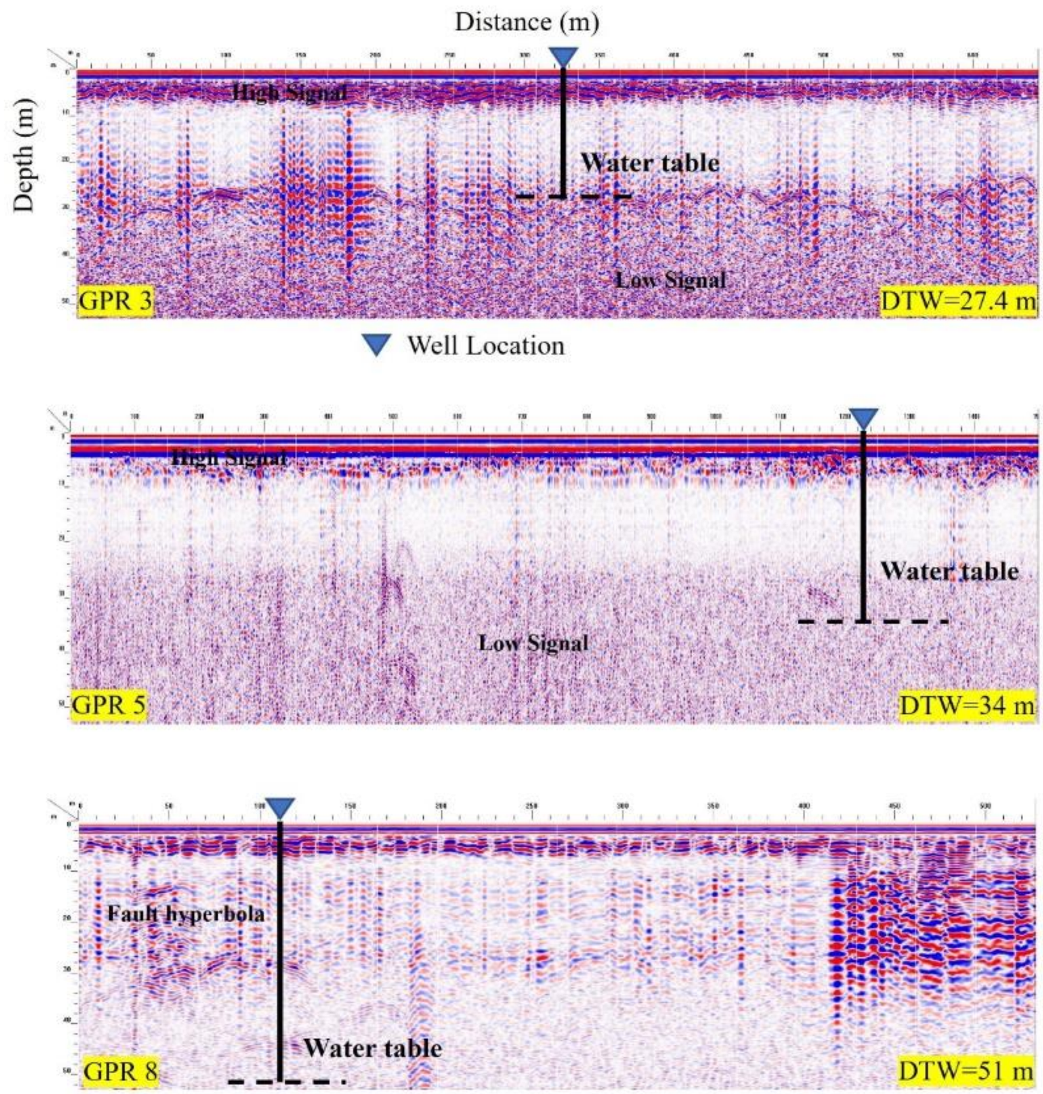

Distance (m)
Depth (m)
High Signal
Water table
Low Signal
GPR 3
DTW=27.4 m
Well Location
High Signal
Water table
Low Signal
GPR 5
DTW=34 m
Fault hyperbola
Water table
GPR 8
DTW=51 m

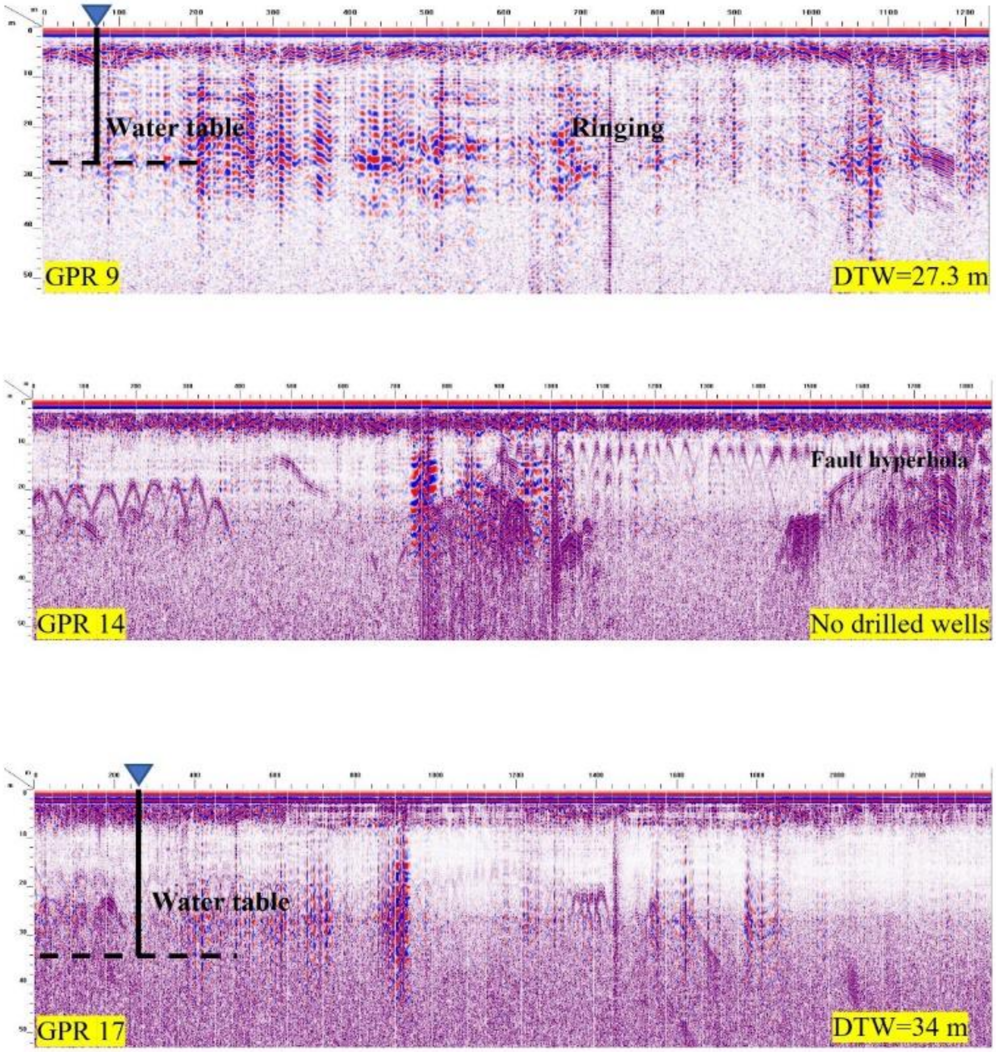


Figure 35: Processed GPR profiles (depth in m along the y-axis, and horizontal distance in m along the x-axis). On these profiles, depth to water table from different wells are marked except profile GPR 14 that has no nearby well. Also, GPR 8 start point is 100 m away from the closest well.

# 5. DISCUSSION AND CONCLUSION

## 5.1 Discussion

Prospecting for groundwater in basement terrain can be challenging due to the limited lateral and vertical extension of aquifers in these rocks. Aquifers in basement terrain typically have distinct characteristics that make groundwater exploration more complex. Basement rocks exhibit high heterogeneity, with variations in lithology, mineralogy, and fracture density. This heterogeneity affects the occurrence and distribution of aquifers, as fractured zones determine groundwater availability. Due to the limited lateral and vertical extension of aquifers in basement terrains, the overall availability of groundwater resources in these rocks may be limited (Fashae et al., 2014; Mohamed et al., 2015). Aquifers in our study area are recharged by both direct and indirect sources. The infiltration of rainfall is the primary source of direct recharge. Infiltration of precipitation and surface runoff occurs primarily through faults and shear zones, resulting in indirect recharge. The topography of the water table is roughly similar to that of the land surface under natural conditions, but with less relief (Derie, 2011). The surface topography can be used to approximate the general direction of groundwater flow.

In this study we integrated remote sensing and geophysical data to map groundwater recharge and extraction areas in the basement terrains of southern Sinai, Egypt. The WOM (Figure 26) was used to identify potential recharge areas. A positive correlation was observed between WOM-derived recharge locations and the distribution of productive wells. Recharge areas are those where the aquifer gets replenished, leading to an increase in its water level and storage. Consequently, high recharge areas often exhibit higher groundwater levels and a greater availability of water within the aquifer.

Faults and shear zones in southern Sinai trend mainly along two main structural trends: NW-SE, and NE–SW (Figure 11). Understanding the characteristics and behavior of these structural elements is crucial for managing and sustainably utilizing groundwater resources in basement aquifers (Mohamed et al., 2015).

Faults and shear zones do create localized areas of enhanced recharge or discharge. When faults intersect the ground surface, they act as natural channels for precipitation to infiltrate into the subsurface, resulting in increased recharge. These areas of focused recharge have a significant influence on groundwater availability and extraction. This relationship between faults, recharge, and groundwater extraction is evident from our WOM results (Figure 26). Our findings show that fault distribution, fault intersection, and the stream network, which are primarily controlled by structural movements, determine the distribution of high potential recharge areas (Figure 26).

The interpretation of geophysical data collected along faults or fault/shear zone intersections (Figures 30 and 34) has confirmed the presence of conductive zones, which represent groundwater-saturated aquifers. The spatial distribution and thickness of these conductive zones are primarily influenced by the structural elements, such as faults and shear zones. These structural features play a significant role in controlling the occurrence and characteristics of the aquifers within the study area.

Faults and shear zones play a crucial role in facilitating groundwater movement by creating pathways and preferential flow paths. They act as high-permeability zones, enabling water to flow more easily along the fault or shear zone. The interconnected fractures and fissures associated with these structures enhance the connectivity of the aquifer. This is supported by the spatial distribution of productive wells in the study area, which align predominantly along these fault and shear zone systems (Figure 24). Furthermore, geophysical surveys have indicated the presence of enhanced saturated zones along these structural elements (Figure 16). These observations provide further evidence of the influence of faults and shear zones on groundwater recharge and extraction in the area.

It is important to acknowledge that faults can possess complex hydrogeological characteristics that have implications for groundwater recharge and extraction (Mohamed et al., 2015). The spatial distribution of primary fracture networks, fault gouge, and crushed zones can impact groundwater flow rates and pathways. This variability in hydrogeological characteristics may contribute to the heterogeneity in groundwater levels and account for differences in productivity between two nearby wells situated along the same fault or shear zone system. Furthermore, this variability may explain the slight differences observed between groundwater levels measured from wells and those obtained from geophysical surveys conducted in close proximity to these wells.

The study had some limitations, including those associated with mapping recharge and extraction locations. Specifically, in our WOM approach, we assigned equal weights to the model inputs. Although our results were validated by spatially correlating them with the distribution of productive wells obtained from published studies, it is important to acknowledge that adjusting the weights assigned to each input layer could potentially influence the model output. By considering different weight combinations, a more comprehensive analysis can be conducted to assess the sensitivity of the results and explore alternative interpretations. Moreover, additional data from complementary techniques are necessary to validate and confirm the results obtained from the WOM method. For instance, incorporating results from stable isotopes analyses and numerical modeling can provide further insights and help verify the findings obtained through the WOM approach. By combining multiple techniques, a more comprehensive and robust understanding of recharge and extraction mapping can be achieved. Stable isotopes of water can be used to trace the origin and movement of groundwater. By analyzing the isotopic composition of water samples from different locations, it is possible to identify areas with a higher contribution of recently recharged water, indicating recharge zones (Ahmed et al., 2022; Isawi et al., 2016). Groundwater flow models can simulate the movement of water in the subsurface and help identify areas with higher recharge rates. By incorporating information on geological properties, hydrological data, and precipitation patterns into the model, it is possible to map the spatial distribution of recharge zones (Abouelmagd et al., 2014; Arnous, 2016). Continuous groundwater level measurements using transducers in wells are a valuable method for monitoring and understanding the behavior of groundwater in basement terrains (Kruseman et al., 1970). Stream flow data helps in the identification of areas with consistent or intermittent high streamflow, indicating the presence of excess surface water. These areas could be potential recharge locations, with excess water diverted or allowed to infiltrate into the ground to replenish aquifers. Furthermore, stream flow data is critical in improving the identification and understanding of recharge locations. We can improve our understanding of recharge processes and predict recharge locations by calibrating the model with observed stream flow data.

The intersections of structural elements (e.g., faults, shear zones) were used to define optimal extraction locations. These elements were mapped from published geologic maps and remote sensing products. Mapping faults from remote sensing data indeed has its limitations. In the specific study conducted, the spatial resolution of the remote sensing data used (30 m) was not sufficient to accurately capture small-scale or narrow faults. As a result, fine-scale fault features were either missed or poorly resolved, leading to incomplete fault mapping. However, it is worth noting that the study focused solely on large-scale structural elements that extend over several kilometers in the field, mitigating the impact of the resolution limitation. The complex geological settings in the southern Sinai region, characterized by multiple rock units, posed challenges in distinguishing faults from other geological features. The presence of features like dikes further contributed to confusion in fault mapping. To address these challenges, the study combined the mapping of faults and shear zones, recognizing the need to consider both structural elements. It is also important to acknowledge that fault mapping from remote sensing data often involves interpretation and subjective analysis. Different analysts may have varying interpretations, leading to inconsistencies in the final fault maps. To enhance the accuracy and reliability of fault mapping, the extracted faults were correlated with high-resolution Google Earth images, providing additional visual information for validation and verification.

The geophysical surveys conducted in the study encountered certain challenges. Specifically, for the VES technique, increasing the AB/2 spacing to achieve greater penetration depth was challenging due to the limited width of the wadies, presence of topographic variations, and ongoing construction activities in the investigation area. These factors limited the ability to optimize the survey configuration for deeper subsurface imaging. A fundamental assumption of the VES method is that the geology is one-dimensional (e.g., z-axis), i.e., it doesn't vary in the two horizontal directions (e.g., x-axis and y-axis) is clearly violated in doing filed work in the wadies and is probably the reason for the relatively large RMS fits, particularly at the larger AB spacings. Furthermore, the coarse-grained sediments flooring the wadi posed difficulties in establishing proper electrode contact with the surface. This led us to repeat these measurements several times and water the electrodes more than once. Additionally, one of the field trips took place during the summer of 2022, when high temperatures were experienced. As a consequence, the Vertical Electrical Sounding (VES) measurements required an extended recording time of up to 20 minutes to obtain a single recording. This prolonged recording time was necessary due to the challenges posed by high temperatures during the summer of 2022. However, despite the extended duration, there were instances where the recorded data provided no real readings, and occasional interruptions occurred during the recording process. To mitigate these issues and improve data reliability, several repeats of the VES measurements were conducted. These repeats aimed to ensure data consistency and enhance the overall quality of the VES data used in the study.

A fundamental assumption of the seismic refraction method is the principle of reciprocity, in which if the positions of the shot point and receiver are switched, the travel times should be the same. This assumption is clearly violated in some of our collected profiles. Three-dimensional subsurface heterogeneities might explain that. This could be the reason for the relatively large RMS fits for these profiles. The seismic refraction surveys conducted in the study had certain challenges as well. Firstly, the use of a hammer as a seismic source for data acquisition had an impact on the data quality. This resulted in the recording of noisy data by the far geophones, which may have affected the accuracy and reliability of the seismic measurements. A shot point at each geophone location was used to mitigate that effect. Additionally, the seismic refraction technique is sensitive to acoustic noise and vibrations, such as those caused by the movement of trucks. These external factors can introduce interference and affect the quality of the recorded seismic data. Our profiles were collected away, as possible, from these sources. Similar to the VES campaign, the presence of coarse grains in the wadi flooring posed challenges in establishing proper geophone contact with the surface. This limitation may have influenced the quality and consistency of the recorded seismic data. Some extremely noisy records were eliminated while processing our seismic data.

There is a discernible difference between the groundwater levels obtained from wells and those derived from our geophysical surveys. This disparity can be attributed to the nature of the transitional interface between unsaturated and saturated sediments, as depicted by the seismic velocity profiles illustrated in Figure 33. The interface between unsaturated and saturated sediments is not a distinct boundary but rather exhibits a gradual transition zone. Research by Si et al. (2016) has indicated that seismic wave velocities become more sensitive when water saturation exceeds 60%, with a pronounced increase in velocities observed at saturations exceeding 90%. The height of the capillary fringe, which experiences variations between dry and wet seasons as highlighted by Ronen et al. (2000), significantly impacts the response of water levels to precipitation events. The capillary fringe, extending above the saturated zone, can reach heights exceeding 2 meters for very fine sands, as reported by Cloke et al. (2006) and Liu et al. (2014). By assessing the height of the capillary fringe, it becomes possible to estimate the type of geological material present within that specific depth zone. This information aids in understanding the observed differences between groundwater levels derived from wells and those inferred from geophysical surveys. It is important to consider the complex interplay between the capillary fringe, the transition zone between unsaturated and saturated sediments, and the influence of seasonal variations when analyzing and interpreting the variations in groundwater levels obtained from different data sources.

## 5.2 Conclusion

Groundwater resources are the only long-term solution for freshwater to sustain the local people living in southern Sinai. We conducted an integrated study using remote sensing data sets, geophysical, and GIS technologies to determine optimal recharge locations and optimal locations for drilling sustainable groundwater wells in Southern Sinai, Egypt. The WOM was used to map potential recharge locations using six input layers: surface lithology, rainfall, slope, stream density, fault density, and fault intersection. These layers are known to have significant impacts on recharge rates in southern Sinai and other similar geologic settings. Model results indicate that 15%, 37%, and 47% of the study area represent high, moderate, and low potential recharge areas, respectively. High potential recharge areas are spatially correlated with those that have porous lithology, relatively high rainfall, high fault density, high stream density, and close to fault intersection. A total of 334 locations were mapped at intersections of two or more fault/shear zones systems, as optimal locations for drilling sustainable groundwater wells. Most of these potential locations were located into the classes of moderate and high potential recharge.

Geophysical surveys (VES, SR, and GPR) have been conducted at the proposed groundwater extraction locations determined from the WOM. These techniques were integrated in order to create, compare, and validate each dataset. The first technique was the VES, which measured the resistivity, thickness of, and depth to saturation zones in five wadies (Elsheikh, Elfuria, Sudud, Isbaeya, and Ghreaba). The second technique was shallow SR, which was carried out close to the VES survey to create a subsurface cross-section showing the different subsurface layers. The third technique was a GPR that was used to generate a continuous record of the top of the water saturation zone. Results of geophysical surveys showed that groundwater-bearing zones (e.g., saturated zones) were restricted to fractures, faults, shear zones, and wadi networks. The groundwater flow within these zones is mainly controlled by surface gradient. Electrical resistivity of unsaturated sediments, saturated sediments, and basement rocks ranges between 830–8700 Ω.m, 220–420 Ω.m, and 1840–26500 Ω.m, respectively. SR velocities of unsaturated sediments, saturated sediments, and basement rocks ranges between 405–547 m/s, 1325–1680 m/s, and 1818–4810 m/s, respectively. The average depth to, and thickness of, saturated zones from SR were in the range of 5–17 m and 14.5–24.5 m, respectively. Based on VES results, the average depth to the saturated zones was in the range of 2–36 m, while the average thickness of the saturated zones was in the range of 2–22 m. Areas where two or more faults and shear zones intersected were found to have thicker and shallower saturated zones. The slight differences between depths to water table in nearby wells (deeper) and these extracted from VES (shallower) are mainly related to the thick capillary fringe in wadi-fill deposits. Unfortunately, the GPR data showed nothing coherent below the first 10-15 m due to the antenna ringing at about 29 MHz.

According to our findings, the intersections of faults or shear zones could be used as a first-order map guide for the distribution of groundwater flow in basement terrains. The proposed integrated (remote sensing, field geophysics, and GIS) methodologies are simple, practical, and cost-effective, and they have the potential to identify the distribution of water resources in many similar fractured basement terrains around the world.

REFERENCES

Abd Ellah, Radwan G. "Water resources in Egypt and their challenges, Lake Nasser case study." The Egyptian Journal of Aquatic Research 46, no. 1 (2020): 1-12.

Abdelrahman, K., Alfaifi, H., Ibrahim, E., Al-Qadasi, B., & Alumidan, S. (2017). Detection of a shallow groundwater aquifer using seismic Refraction tomography: A case study of Wadi Showat, Abha District, southern Saudi Arabia. SEG Technical Program Expanded Abstracts, 5418–5421. https://doi.org/10.1190/segam2017-17738517.1

Abdin, A. E., & Gaafar, I. (2009). Rational Water Use in Egypt. Series A – Mediterranean Seminars, No. 88, Technological Perspectives for Rational Use of Water Resources in the Mediterranean Region, 27(December 2009), 11–27.

Abo-El-Fadl. (2013). Possibilities of Groundwater Pollution in Some Areas, East of Nile Delta, Egypt. International Journal of Environment, 1(1), 1–21.

Abouelmagd, A. (2003). Quantitative hydrogeological studies onWadi Feiran basin, South Sinai, with emphasis on the prevailing environmental conditions. MSc Thesis, Suez Canal University, Ismailia, Egypt.

Abouelmagd, Abdou, Sultan, M., Sturchio, N. C., Soliman, F., Rashed, M., Ahmed, M., Kehew, A. E., Milewski, A., & Chouinard, K. (2014). Paleoclimate record in the Nubian Sandstone Aquifer, Sinai Peninsula, Egypt. Quaternary Research (United States), 81(1), 158–167. https://doi.org/10.1016/j.yqres.2013.10.017

Adelinet, M., Domínguez, C., Fortin, J., & Violette, S. (2018). Seismic-refraction field experiments on Galapagos Islands: A quantitative tool for hydrogeology. Journal of Applied Geophysics, 148, 139–151. https://doi.org/10.1016/j.jappgeo.2017.10.009

Ahmed, M., Chen, Y., & Khalil, M. M. (2022). Isotopic composition of groundwater resources in arid environments. Journal of Hydrology, 609(September 2021), 127773. https://doi.org/10.1016/j.jhydrol.2022.127773

Amer, R., Sultan, M., Ripperdan, R., Ghulam, A., & Kusky, T. (2013). An integrated approach for groundwater potential zoning in shallow fracture zone aquifers. International Journal of Remote Sensing, 34(19), 6539–6561. https://doi.org/10.1080/01431161.2013.804221

Araffa, S. A. S., Mohamed, A. M. E., & Santos, F. M. (2017). Geophysical investigation in the Northwestern part of the Gulf of Suez, Egypt. Egyptian Journal of Petroleum, 26(2), 457–475. https://doi.org/10.1016/j.ejpe.2016.06.002

Arnous, M. O. (2016a). Cartographie des potentialités des aquifères en terrains de socle en régions arides à partir de la modélisation géospatiale: exemple du bassin du Wadi Feiran, Sud Sinaï, Egypte. Hydrogeology Journal, 24(6), 1375–1392. https://doi.org/10.1007/s10040-016-1417-8

Arnous, M. O. (2016b). Cartographie des potentialités des aquifères en terrains de socle en régions arides à partir de la modélisation géospatiale: exemple du bassin du Wadi Feiran, Sud Sinaï, Egypte. Hydrogeology Journal, 24(6), 1375–1392. https://doi.org/10.1007/S10040-016-1417-8/FIGURES/14

Arulbalaji, P., Sreelash, K., Maya, K., & Padmalal, D. (2019). Hydrological assessment of groundwater potential zones of Cauvery River Basin, India: a geospatial approach. Environmental Earth Sciences, 78(24), 1–21. https://doi.org/10.1007/s12665-019-8673-6

Awadallah, A. G., Magdy, M., Helmy, E., & Rashed, E. (2017). Assessment of rainfall intensity equations enlisted in the egyptian code for designing potable water and sewage networks. Advances in Meteorology, 2017(2). https://doi.org/10.1155/2017/9496787

Azhar, A. S. bin, Latiff, A. H. A., Lim, L. H., & Gödeke, S. H. (2019). Groundwater investigation of a coastal aquifer in Brunei Darussalam using seismic refraction. Environmental Earth Sciences, 78(6), 1–17. https://doi.org/10.1007/s12665-019-8203-6

Babiker, M., & Gudmundsson, A. (2004). The effects of dykes and faults on groundwater flow in an arid land: The Red Sea Hills, Sudan. Journal of Hydrology, 297(1–4), 256–273. https://doi.org/10.1016/j.jhydrol.2004.04.018

Becht, A., Bürger, C., Kostic, B., Appel, E., & Dietrich, P. (2007). High-resolution aquifer characterization using seismic cross-hole tomography: An evaluation experiment in a gravel delta. Journal of Hydrology, 336(1–2), 171–185. https://doi.org/10.1016/j.jhydrol.2007.01.005

Blenkinsop, T. G., & Kadzviti, S. (2006). Fluid flow in shear zones: Insights from the geometry and evolution of ore bodies at Renco gold mine, Zimbabwe. Geofluids, 6(4), 334–345. https://doi.org/10.1111/j.1468-8123.2006.00154.x

Caine, J. S., Evans, J. P., & Forster, C. B. (1996). Fault zone architecture and permeability structure. Geology, 24(11), 1025–1028. https://doi.org/10.1130/0091-7613(1996)024<1025:FZAAPS>2.3.CO;2

Chen, C. Sen, Lin, Y. L., Zeng, H. T., Chen, C. Y., & Liu, C. L. (2013). Orographic effects on heavy rainfall events over northeastern Taiwan during the northeasterly monsoon season. Atmospheric Research, 122, 310–335. https://doi.org/10.1016/j.atmosres.2012.10.008

Cloke, H. L., Anderson, M. G., McDonnell, J. J., & Renaud, J. P. (2006). Using numerical modelling to evaluate the capillary fringe groundwater ridging hypothesis of streamflow generation. Journal of Hydrology, 316(1–4), 141–162. https://doi.org/10.1016/j.jhydrol.2005.04.017

Cooper, M. (2010). Advanced Bash-Scripting Guide An in-depth exploration of the art of shell scripting Table of Contents. Okt 2005 Abrufbar Uber Httpwww Tldp OrgLDPabsabsguide Pdf Zugriff 1112 2005, 2274(November 2008), 2267–2274. https://doi.org/10.1002/hyp

DAVIS, J. L., & ANNAN, A. P. (1989). Ground-Penetrating Radar for High-Resolution Mapping of Soil and Rock Stratigraphy. Geophysical Prospecting, 37(5), 531–551. https://doi.org/10.1111/j.1365-2478.1989.tb02221.x

Derie, B. (2011). Integration of geophysical methods for groundwater exploration in hard rock areas : application to Alla Valley , Eritrea , NE Africa.

Desper, D. B., Link, C. A., & Nelson, P. N. (2015). Accurate water-table depth estimation using seismic refraction in areas of rapidly varying subsurface conditions. Near Surface Geophysics, 13(5), 455–465. https://doi.org/10.3997/1873-0604.2015039

Djuma, H., Bruggeman, A., Eliades, M., & Lange, M. A. (2016). Non-conventional water resources research in semi-arid countries of the Middle East. Desalination and Water Treatment, 57(5), 2290–2303. https://doi.org/10.1080/19443994.2014.984930

Doolittle, J. A., Jenkinson, B., Hopkins, D., Ulmer, M., & Tuttle, W. (2006). Hydropedological investigations with ground-penetrating radar (GPR): Estimating water-table depths and local ground-water flow pattern in areas of coarse-textured soils. Geoderma, 131(3–4), 317–329. https://doi.org/10.1016/j.geoderma.2005.03.027

Drisya, J. (2016). Comparison of digitally delineated stream networks from different spaceborne digital elevation models: A case study based on two watersheds in South India. Arabian Journal of Geosciences, 9(18). https://doi.org/10.1007/s12517-016-2726-x

El-Rayes, A. (1992). Hydrogeological studies of Saint Katherine area, South Sinai, Egypt. MSc Thesis, Suez Canal University, Ismailia, Egypt.

EL-Rayes, A. E., Arnous, M. O., & Aboulela, H. A. (2015). Hydrogeochemical and seismological exploration for geothermal resources in South Sinai, Egypt utilizing GIS and remote sensing. Arabian Journal of Geosciences, 8(8), 5631–5647. https://doi.org/10.1007/s12517-014-1667-5

El-Sayed, M. M. (2006). Geochemistry and petrogenesis of the post-orogenic bimodal dyke swarms in NW Sinai, Egypt: constraints on the magmatic-tectonic processes during the late Precambrian. Chemie Der Erde - Geochemistry, 66(2), 129–141. https://doi.org/10.1016/j.chemer.2003.12.003

El-Shafei, M. K., & Kusky, T. M. (2003). Structural and tectonic evolution of the Neoproterozoic Feiran-Solaf metamorphic belt, Sinai Peninsula: Implications for the closure of the Mozambique Ocean. Precambrian Research, 123(2–4), 269–293. https://doi.org/10.1016/S0301-9268(03)00072-X

Elewa, H. H., & Qaddah, A. A. (2011). Groundwater potentiality mapping in the Sinai Peninsula, Egypt, using remote sensing and GIS-watershed-based modeling. Hydrogeology Journal, 19(3), 613–628. https://doi.org/10.1007/s10040-011-0703-8

Essam, D., Ahmed, M., Abouelmagd, A., & Soliman, F. (2020). Monitoring temporal variations in groundwater levels in urban areas using ground penetrating radar. Science of the Total Environment, 703. https://doi.org/10.1016/j.scitotenv.2019.134986

Evans, J. P., Forster, C. B., & Goddard, J. V. (1997). Permeability of fault-related rocks, and implications for hydraulic structure of fault zones. Journal of Structural Geology, 19(11), 1393–1404. https://doi.org/10.1016/S0191-8141(97)00057-6

Faheem, H., Khattak, Z., Islam, F., Ali, R., Khan, R., Khan, I., & Tag Eldin, E. (2023). Groundwater potential zone mapping using geographic information systems and multi-influencing factors: A case study of the Kohat District, Khyber Pakhtunkhwa. Frontiers in

Earth Science, 11(January), 1–18. https://doi.org/10.3389/feart.2023.1097484

Fashae, O. A., Tijani, M. N., Talabi, A. O., & Adedeji, O. I. (2014). Delineation of groundwater potential zones in the crystalline basement terrain of SW-Nigeria: an integrated GIS and remote sensing approach. Applied Water Science, 4(1), 19–38. https://doi.org/10.1007/s13201-013-0127-9

Fatema, K., Joy, M. A. R., Amin, F. M. R., & Sarkar, S. K. (2023). Groundwater potential mapping in Jashore, Bangladesh. Heliyon, 9(3), e13966. https://doi.org/10.1016/j.heliyon.2023.e13966

Fried, A., & Serio, B. (2012). Water Industry Segment Report Desalination. July, 1–35. www.wtcsd.org

Gaber, G. M., Saleh, S., & Toni, M. (2022). Crustal thickness and structural pattern evaluation of Sinai Peninsula using three-dimensional density modeling with aeromagnetic and earthquake data. Acta Geophysica, 70(2), 639–657. https://doi.org/10.1007/s11600-022-00744-4

Genedi, M. A., & Youssef, M. A. S. (2023). Application of geophysical techniques for shallow groundwater investigation using 1D - lateral constrained and 2D inversions in Ras Gara area , southwestern Sinai , Egypt. Environmental Earth Sciences, 82(5), 1–17. https://doi.org/10.1007/s12665-023-10796-4

Goddard, J. V., & Evans, J. P. (1995). Chemical changes and fluid-rock interaction in faults of crystalline thrust sheets, northwestern Wyoming, U.S.A. Journal of Structural Geology, 17(4), 533–547. https://doi.org/10.1016/0191-8141(94)00068-B

Grelle, G., & Guadagno, F. M. (2009). Seismic refraction methodology for groundwater level determination: "Water seismic index." Journal of Applied Geophysics, 68(3), 301–320.

https://doi.org/10.1016/j.jappgeo.2009.02.001

Gudmundsson, A. (2000). Active fault zones and groundwater flow. Geophysical Research Letters, 27(18), 2993–2996. https://doi.org/10.1029/1999GL011266

Haeni, F. P. (1988). Application of seismic-refraction techniques to hydrologic studies. US Geological Survey, Techniques of Water-Resources Investigations, BK2 Ch D2.

Hamed, M. M., Nashwan, M. S., & Shahid, S. (2022). Climatic zonation of Egypt based on high-resolution dataset using image clustering technique. Progress in Earth and Planetary Science, 9(1). https://doi.org/10.1186/s40645-022-00494-3

Hou, A. Y., Kakar, R. K., Neeck, S., Azarbarzin, A. A., Kummerow, C. D., Kojima, M., Oki, R., Nakamura, K., & Iguchi, T. (2014). The global precipitation measurement mission. Bulletin of the American Meteorological Society, 95(5), 701–722. https://doi.org/10.1175/BAMS-D-13-00164.1

Houze, R. A. (2012). Orographic effects on precipitating clouds. Reviews of Geophysics, 50(1), 1–47. https://doi.org/10.1029/2011RG000365

Huffman, G. J., Gsfc, N., Bolvin, D. T., Braithwaite, D., Hsu, K., Joyce, R., Kidd, C., Nelkin, E. J., Sorooshian, S., Tan, J., & Xie, P. (2019). NASA Global Precipitation Measurement (GPM) Integrated Multi-satellitE Retrievals for GPM (IMERG). Algorithm Theoretical Basis Document (ATBD) Version 06, November.

Isawi, H., El-Sayed, M. H., Eissa, M., Shouakar-Stash, O., Shawky, H., & Abdel Mottaleb, M. S. (2016). Integrated Geochemistry, Isotopes, and Geostatistical Techniques to Investigate Groundwater Sources and Salinization Origin in the Sharm EL-Shiekh Area, South Sinia, Egypt. Water, Air, and Soil Pollution, 227(5). https://doi.org/10.1007/s11270-016-2848-5

Issar & Gilad, 1982. (1982). Groundwater flow systems in the arid crystalline province of southern sinai. Hydrological Sciences Journal, 27(3), 309–325. https://doi.org/10.1080/02626668209491112

Kabesh, M., Asran, A. M., & Rahman, E. A. (2013). Mineral chemistry of banded migmatites from Hafafit and Feiran areas, Egypt. Arabian Journal of Geosciences, 6(10), 3669–3681. https://doi.org/10.1007/s12517-012-0628-0

Kaewdum, N., & Chotpantarat, S. (2021). Mapping Potential Zones for Groundwater Recharge Using a GIS Technique in the Lower Khwae Hanuman Sub-Basin Area, Prachin Buri Province, Thailand. Frontiers in Earth Science, 9(September), 1–16. https://doi.org/10.3389/feart.2021.717313

Kameri, P., Kameri, P., Kameri, P., Úrsula, B., Spring, O., Grin, J., Mesjasz, C., Kameri, P., Navnita, -Mbote, Behera, C., Chourou, B., & Krummenacher, H. (n.d.). VOL 4 / HEXAGON SERIES ON HUMAN AND ENVIRONMENTAL SECURITY AND PEACE ch Spring in asz Mbote era rou nacher s.) Facing Global Environmental Change (Vol. 4).

Karimi, D., Bahrami, J., Mobaraki, J., Missimer, T. M., & Taheri, K. (2022). Groundwater sustainability assessment based on socio-economic and environmental variables: a simple dynamic indicator-based approach. Hydrogeology Journal, 30(7), 1963–1988. https://doi.org/10.1007/s10040-022-02512-6

Khalil, M. H., Hanafy, S. M., & Gamal, M. A. (2008). Preliminary seismic hazard assessment, shallow seismic refraction and resistivity sounding studies for future urban planning at the Gebel Umm Baraqa area, Egypt. Journal of Geophysics and Engineering, 5(4), 371–386. https://doi.org/10.1088/1742-2132/5/4/002

Kim, H. S., & Kim, J. Y. (2008). High-resolution profiling of alluvial aquifer in potential riverbank filtration site by use of combining CMP refraction and reflection seismic methods. Journal of Applied Geophysics, 66(1–2), 1–14. https://doi.org/10.1016/j.jappgeo.2008.08.003

Liu, Q., Yasufuku, N., Miao, J., & Ren, J. (2014). An approach for quick estimation of maximum height of capillary rise. Soils and Foundations, 54(6), 1241–1245. https://doi.org/10.1016/j.sandf.2014.11.017

Lowrie, W. (2007). Fundamentals Of Geophysics, Second Edition. In Cambridge University Press.

Mahmoudzadeh, M. R., Francés, A. P., Lubczynski, M., & Lambot, S. (2012). Using ground penetrating radar to investigate the water table depth in weathered granites - Sardon case study, Spain. Journal of Applied Geophysics, 79, 17–26. https://doi.org/10.1016/j.jappgeo.2011.12.009

Mandal, P., Saha, J., Bhattacharya, S., & Paul, S. (2021). Delineation of groundwater potential zones using the integration of geospatial and MIF techniques: A case study on Rarh region of West Bengal, India. Environmental Challenges, 5(November), 100396. https://doi.org/10.1016/j.envc.2021.100396

Mohamaden, M. I. I., El-Sayed, H. M., & Hamouda, A. Z. (2016). Combined application of electrical resistivity and GIS for subsurface mapping and groundwater exploration at El-Themed, Southeast Sinai, Egypt. Egyptian Journal of Aquatic Research, 42(4), 417–426. https://doi.org/10.1016/j.ejar.2016.10.007

Mohamed, L. (2015). Structural Controls on the Distribution of Groundwater in Southern Sinai, Egypt: Constraints from Geophysical and Remote Sensing Observations. 1, 77 pp. http://scholarworks.wmich.edu/dissertations

Mohamed, L., Sultan, M., Ahmed, M., Zaki, A., Sauck, W., Soliman, F., Yan, E., Elkadiri, R., &

Abouelmagd, A. (2015a). Structural Controls on Groundwater Flow in Basement Terrains: Geophysical, Remote Sensing, and Field Investigations in Sinai. Surveys in Geophysics, 36(5), 717–742. https://doi.org/10.1007/s10712-015-9331-5

Mohamed, L., Sultan, M., Ahmed, M., Zaki, A., Sauck, W., Soliman, F., Yan, E., Elkadiri, R., & Abouelmagd, A. (2015b). Structural Controls on Groundwater Flow in Basement Terrains: Geophysical, Remote Sensing, and Field Investigations in Sinai. Surveys in Geophysics, 36(5), 717–742. https://doi.org/10.1007/s10712-015-9331-5

Murad, A., Baker, H., Mahmoud, S., & Gabr, A. (2014). Detecting Groundwater Levels Using the Shallow Seismic Method: Case Study. Journal of Hydrologic Engineering, 19(5), 867–876. https://doi.org/10.1061/(asce)he.1943-5584.0000791

Nasir, M. J., Khan, S., Ayaz, T., Khan, A. Z., Ahmad, W., & Lei, M. (2021). An integrated geospatial multi-influencing factor approach to delineate and identify groundwater potential zones in Kabul Province, Afghanistan. Environmental Earth Sciences, 80(13), 1–13. https://doi.org/10.1007/s12665-021-09742-z

Nasir, M. J., Khan, S., Zahid, H., & Khan, A. (2018). Delineation of groundwater potential zones using GIS and multi influence factor (MIF) techniques: a study of district Swat, Khyber Pakhtunkhwa, Pakistan. Environmental Earth Sciences, 77(10), 1–11. https://doi.org/10.1007/s12665-018-7522-3

Neev, D. (1975). Tectonic evolution of the Middle East and the Levantine basin (easternmost Mediterranean). Geology, 3(12), 683–686. https://doi.org/10.1130/0091-7613(1975)3<683:TEOTME>2.0.CO;2

Olayinka, A. I. (1992). Geophysical siting of boreholes in crystalline basement areas of Africa. Journal of African Earth Sciences, 14(2), 197–207. https://doi.org/10.1016/0899-

5362(92)90097-V

Pasquet, S., Bodet, L., Dhemaied, A., Mouhri, A., Vitale, Q., Rejiba, F., Flipo, N., & Guérin, R. (2015). Detecting different water table levels in a shallow aquifer with combined P-, surface and SH-wave surveys: Insights from VP/VS or Poisson's ratios. Journal of Applied Geophysics, 113, 38–50. https://doi.org/10.1016/j.jappgeo.2014.12.005

Paz, A. R., & Collischonn, W. (2007). River reach length and slope estimates for large-scale hydrological models based on a relatively high-resolution digital elevation model. Journal of Hydrology, 343(3–4), 127–139. https://doi.org/10.1016/j.jhydrol.2007.06.006

Ronen, D., Scher, H., & Blunt, M. (2000). Field observations of a capillary fringe before and after a rainy season. Journal of Contaminant Hydrology, 44(2), 103–118. https://doi.org/10.1016/S0169-7722(00)00096-6

Sharp, I. R., Gawthorpe, R. L., Underhill, J. R., & Gupta, S. (2000). Fault-propagation folding in extensional settings: Examples of structural style and synrift sedimentary response from the Suez rift, Sinai, Egypt. Bulletin of the Geological Society of America, 112(12), 1877–1899. https://doi.org/10.1130/0016-7606(2000)112<1877:FPFIES>2.0.CO;2

Shen, Y., & Xiong, A. (2016). Validation and comparison of a new gauge-based precipitation analysis over mainland China. International Journal of Climatology, 36(1), 252–265. https://doi.org/10.1002/joc.4341

Shendi, E H, & Abouelmagd,  a a. (2004). New aprroach for ground geophysics in the development of groundwater in the basement terrains ( A case study from south Sinai , Egypt ). Proceeding of the 7th Conf. GEOLOGY of Sinai for Development Ismailia, Acworth 1987, 129–140.

Shendi, Elarabi H, & El-Rayes, A. (1992). Geophysical prospecting for groundwater in Wadi

Sibaiya-Wadi El-Sheikh area, south Sinai. MERC Ain Shams Univ Earth Sci Ser, 6, 55–61.

Si, W., Di, B., Wei, J., & Li, Q. (2016). Journal of Natural Gas Science and Engineering Experimental study of water saturation effect on acoustic velocity of sandstones. Journal of Natural Gas Science and Engineering, 33, 37–43. https://doi.org/10.1016/j.jngse.2016.05.002

Sultan, M., Arvidson, R. E., Sturchio, N. C., & Guinness, E. A. (1987). Lithologic mapping in arid regions with Landsat thematic mapper data: Meatiq dome, Egypt. Geological Society of America Bulletin, 99(6), 748–762. https://doi.org/10.1130/0016-7606(1987)99<748:LMIARW>2.0.CO;2

Sultan, M., Wagdy, A., Manocha, N., Sauck, W., Gelil, K. A., Youssef, A. F., Becker, R., Milewski, A., El Alfy, Z., & Jones, C. (2008). An integrated approach for identifying aquifers in transcurrent fault systems: The Najd shear system of the Arabian Nubian shield. Journal of Hydrology, 349(3–4), 475–488. https://doi.org/10.1016/j.jhydrol.2007.11.029

Sultan, M., Yan, E., Sturchio, N., Wagdy, A., Abdel Gelil, K., Becker, R., Manocha, N., & Milewski, A. (2007). Natural discharge: A key to sustainable utilization of fossil groundwater. Journal of Hydrology, 335(1–2), 25–36. https://doi.org/10.1016/j.jhydrol.2006.10.034

Sultan, M., Yousef, A. F., Metwally, S. E., Becker, R., Milewski, A., Sauck, W., Sturchio, N. C., Mohamed, A. M. M., Wagdy, A., Alfy, Z. El, Soliman, F., Rashed, M., Becker, D., Sagintayev, Z., Ahmed, M., & Welton, B. (2011). Red Sea rifting controls on aquifer distribution: Constraints from geochemical, geophysical, and remote sensing data. Bulletin of the Geological Society of America, 123(5), 911–924. https://doi.org/10.1130/B30146.1

Sultan, Mohamed, Arvidson, R. E., Duncan, I. J., Louis, S., & Stern, R. J. (2000). AREA. 7(6), 1291–1306.

Unit, C., & Sciences, H. (2012). Research Journal of Physics. Academic Journal, Inc., 3(2), 101–112.

Urish, D. W., & Frohlich, R. K. (1990). Surface electrical resistivity in coastal groundwater exploration. Geoexploration, 26(4), 267–289. https://doi.org/10.1016/0016-7142(90)90008-G

van Dam, R. L., & Schlager, W. (2000). Identifying causes of ground-penetrating radar reflections using time-domain reflectometry and sedimentological analyses. Sedimentology, 47(2), 435–449. https://doi.org/10.1046/j.1365-3091.2000.00304.x

Zimik, H. V., Angchuk, T., Misra, A. K., Ranjan, R. K., Wanjari, N., & Basnett, S. (2022). GIS-based identification of potential watershed recharge zones using analytic hierarchy process in Sikkim Himalayan region. Applied Water Science, 12(11), 1–18. https://doi.org/10.1007/s13201-022-01758-5